

DISTRIBUTION STATEMENT A
Approved for Public Release
Distribution Unlimited

Copy 31 of 40
Series 1

REPORT ARC-R-176

THE ROTORNET:
A HIGH-PERFORMANCE HYPERSONIC
DECELERATOR FOR PLANETARY ENTRY

Submitted under Contract NAS7-272

14 February 1965

**Reproduced From
Best Available Copy**

Prepared by:

A. C. Kyser
A. C. Kyser

Approved by:

H. U. Schuerch
H. U. Schuerch

ASTRO RESEARCH CORPORATION
P.O. Box 4128 • Santa Barbara, California
Telephone: 963-3423

20000510 061

ABSTRACT

This report describes the Rotornet, a new type of aerodynamic decelerator proposed for space missions requiring entry into planetary atmospheres. The basic element of the Rotornet is a large, light-weight, flexible, filamentary disk which is attached at its center to a hub on the nose of the entry vehicle, and stiffened, during operation, by a high spin rate. This concept makes possible the use of very large surface areas for aerodynamic braking ($W/C_D A$ less than 1 lb/ft^2). For such low values of $W/C_D A$, the maximum heating rates, even for earth entry at superorbital speeds, are well within the capability of high-temperature filamentary structural materials to reject heat by radiation. Since no non-structural thermal-protection material is required, the decelerator weight can be reduced to a few percent of the payload weight. The mechanical and operational characteristics of the Rotornet are discussed, including its behavior in a hypersonic windstream, and its potential performance as a re-entry decelerator. It is shown that for a given set of entry conditions the ratio of rotor mass to payload mass is proportional to disk radius, which, in turn, is proportional to the cube root of the total vehicle mass; for a 10-g ballistic entry from earth orbit, a rotor weight of about 200 lbs is sufficient for a payload of 10,000 lbs. Finally, the possibilities are discussed for future use of the Rotornet as a decelerator for more severe entry missions.

	<u>Page</u>	
SECTION X	MECHANICAL DESIGN CONSIDERATIONS	50
SECTION XI	POSSIBILITIES FOR THE FUTURE	54
SECTION XII	CONCLUSIONS	57
REFERENCES		58

LIST OF ILLUSTRATIONS

<u>Figure No.</u>	<u>Title</u>	<u>Page</u>
1	Rotornet Decelerator	60
2	General Arrangement	60
3	Operational Sequence	61
4	Adaptation of Isotensoid Disk to Rotornet	61
5	Geodesic Development of Isotensoid Disk	62
6	Stress Distribution in Truncated Disk with Various Sizes of Tip Weights	62
7	Meridional Curves for Coned-Up Rotornet	63
8	Coning Angle Distribution	63
9	Tension Distribution	64
10	Axial Equilibrium at the Hub	64
11	Drag Coefficient vs. Coning Angle (Referred to area of flat disk)	65
12	Coning Angle vs. Loading	65
13	Equilibrium Temperature vs. Heating Rate	66
14	Heating Distributions for Blunt Shapes, Normalized to Stagnation-Point Heating on a Sphere	66
15	Heating Rate and Temperature Distributions on Disk and Shallow Cone	67
16	Coordinate System for Equations of Motion for Entry Vehicle	67
17	Ballistic Trajectory for Earth Entry with Constant Margin of Safety	68
	a. Vehicle Motion	68
	b. Rotornet Response	68
18	Maximum Temperature During Ballistic Entry vs. Heating Parameter	69
19	Spin Rate and Coning Angle for Spin Decay Operation Compared With Constant Margin Operation	69

<u>Figure No.</u>	<u>Title</u>	<u>Page</u>
20	Rotornet Radius for Ballistic Entry	70
21	Rotornet Weight Fraction for Ballistic Entry (Silica fiber with safety factor of 5)	70
22	Rotornet Size vs. Initial Velocity for 10,000 Vehicle (10'g's, 1600°F, Silica, SF=5)	71
23	Rotornet Size vs. Maximum Load Factor for 10,000 lb Vehicle (36,000 ft/sec, 1600°F, Silica, SF=5)	71
24	Rotornet Size vs. Maximum Temperature for 10,000 lb Vehicle (36,000 ft/sec, 10 g's, Silica, SF=5)	72
25	Rotornet Weight Fraction for Ballistic Entry (Rene' 41 with safety factory of 2.5)	72
26	Rotornet Size vs. Initial Velocity for 10,000 lb Vehicle (10 g's, 1600°F, Rene' 41, SF=2.5)	73
27	Rotornet Size vs. Maximum Load Factor for 10,000 lb Vehicle (36,000 ft/sec, 1600°F, Rene' 41, SF=2.5)	73
28	Rotornet Size vs. Maximum Temperature for 10,000 lb Vehicle (36,000 ft/sec, 10 g's, Rene' 41, SF=2.5)	74
29	Conditions for Equilibrium Glide	74
30	Maximum Temperature vs. Load Density	75
31	Strength vs. Temperature for Structural Fibers	75
32	Temperature-Weight Performance Parameter $(\sigma \tau)^{4/3} \lambda_{ult}$ vs. Temperature	76
33	Out-of-Plane Vibration of a Flat Isotensoid Disk: Mode Shape for First Mode	76
34	In-Plane (Tangential) Vibration of a Flat Iso- tensoid Disk: Mode Shape for First Mode	77
35	Vibration of a Coned-Up Rotornet: Mode Shape for First Flapping Mode	77
36	Vibration of a Coned-Up Rotornet: Mode Shape for First Tangential Mode	78

<u>Figure No.</u>	<u>Title</u>	<u>Page</u>
37	Boundary for Catastrophic Flutter	78
38	Effect of Actuator Gain on Stability of Spiral Mode	79
39	Effect of Stability Augmentation Parameters	79
40	Typical Basket-Weave Construction with Parallel Fiber Tapes	80
41	Fabrication of Rotornet by Basket-Weaving Tapes Over a Cylinder Form	80
42	Fabrication of Rotornet by Braiding Tapes on a Continuous Belt	81
43	Rotating Hub Structure	81
44	Deployment of Rotornet	82
45	Mars Landing Probe Mission	82
46	Rotornet Design for Entry on Mars at 90° and 25,000 ft/sec	83
47	Fixed-Offset Glide Vehicle	83

LIST OF SYMBOLS

A	-	surface area; area of flat rotor, ft ²
a_f	-	total cross sectional area of structural fibers, in ²
B	-	aerodynamic loading parameter $\equiv \frac{\rho u^2 \cdot \pi R^2}{\omega^2 R m_R}$
b	-	hub radius, ft
C_p	-	normal pressure coefficient
C_D	-	drag coefficient, based on area of flat disk
C_L	-	lift coefficient
D	-	aerodynamic drag force, lb
e	-	logarithm base
F_b	-	axial component of rotor tension at the hub, lb
g	-	acceleration due to gravity, ft/sec ²
H	-	angular momentum, slug ft ² /sec
h	-	altitude, ft
h_s	-	density scale height, ft
I	-	moment of inertia, slug ft ²
K	-	heating rate coefficient for rim of cone
k	-	coefficient for \dot{q}^2 for given condition
L	-	aerodynamic lift force, lb
l	-	fiber length, ft
M. S.	-	margin of safety for structural fiber
m	-	mass; mass of vehicle, slugs
N	-	load factor $\equiv \dot{u}/g$
n	-	entry parameter $\equiv u^2/rg$
p	-	pressure, lb/ft ²
\dot{q}	-	heating rate; convective heating rate at rim of rotor, Btu/ft ² sec.

R	-	radius; outside radius of rotor, ft
r	-	radius coordinate, ft
s	-	stress in fiber (based on structural cross section) lb/in ²
S.F.	-	factor of safety
T	-	torque, lb/ft
t	-	time, sec
t _e	-	effective (solid) thickness of cylindrical develop- ment of rotor disk, inch
t _{sq}	-	actual thickness of cylindrical development, as- suming square packing, inch
U	-	orbit velocity $\equiv \sqrt{rg} \cong 26,000$ ft/sec
u	-	vehicle velocity, ft/sec
u _t , u _s	-	tangential- and meridional-direction displacements in vibrating rotor
VF	-	effective "view factor" for radiation cooling
W	-	weight; weight of vehicle, lb
w	-	displacement of vibrating rotor, normal to surface
X	-	vehicle dimension for heating, ft
z	-	axial coordinate, from hub plane, ft
β	-	coning angle, degrees
γ	-	angle between fiber and meridian, degrees
ϵ	-	emissivity
θ	-	trajectory flight-path angle, degrees
λ	-	specific strength of structural fiber $\equiv \frac{s}{\rho_f g}$, ft
μ	-	viscosity, lb sec/ft ²
ρ	-	density; density of air, slugs/ft ³
σ	-	Stefan-Boltzmann constant
τ	-	temperature, °R (unless specified as °F)

- ω - spin rate of rotor, rad/sec
- $\bar{\omega}$ - vibration frequency, cycles/revolution

Subscripts

- b - property at hub
- c - property of cone, periphery of cone
- cyl - property of cylindrical development of disk
- e - effective
- F - friction
- f - property of structural fiber
- i - initial condition
- N - condition at time of maximum deceleration
- P - property of payload
- R - property of rotor
- ref - reference; property of isotensoid disk
- rad - radiation
- S - property of stagnation-point on sphere
- tip - property at tip (periphery) of rotor
- ult - ultimate
- τ - condition at time of maximum temperature
- ∞ - condition in undisturbed flow

I. INTRODUCTION

The possibility of using low-wing-loading decelerators for entry from orbit into planetary atmospheres has been of continuing interest since the beginning of serious work in reentry mechanics. Eggers (Reference 1) and Gazley (Reference 2), as well as other early investigators, have pointed out that the maximum heating rate for a given size vehicle decreases with decreases in the ballistic parameter $W/C_D A$; thus, if $W/C_D A$ can be made sufficiently low, the heating rates can be made compatible with the ability of structural materials to reject heat by radiation. A cursory examination of the problem will show that, for typical payload masses, the decelerator surface area required to enter the earth's atmosphere from orbit at practicable temperatures is no greater than that required in the way of a parachute for terminal descent.

The principal advantage to be gained from the low-wing-loading approach is that for a wide range of mission parameters it offers a potentially large decrease in the decelerator mass fraction (ratio of decelerator mass to payload mass) over the use of systems with conventionally high $W/C_D A$. Attendant to this feature, however are a large number of important secondary advantages, such as operation at lower temperatures, improved communication throughout the descent, and a potential for gliding and maneuvering without large increases in structural weight.

Most of the devices which have been proposed to take advantage of this operating regime have had the form of the towed decelerator (e. g., parachutes, balloons, Ballutes, cones, paragliders (Reference 3)). These devices share a number of basic problems; for example, they must operate in the unsteady wake of the payload, and they experience excessive and uneven heating on shroud lines and points of shock impingement.

Furthermore, those shapes which have high drag coefficients are characterized by exposed shroud lines and leading edges, while those having only central support are not blunt bodies and are therefore subject to the high heating rates associated with supersonic boundary layers. In addition, those schemes using completely flexible canopies have encountered difficulty during deployment (opening loads and lack of reliability in the hypersonic regime), while those having structural stiffness have been either difficult to package or dependent on internal pressure. The net result of these efforts has been that, at least for the reentry problem, the radiation-cooled, low $W/C_D A$ decelerator has not been competitive with the ablation-cooled systems.

There have been at least two important attempts to explore the middle ground between these extremes with hybrid systems which have relatively large surface areas but which depend to some extent on ablative protection. With the Avco Drag Brake (Reference 4) many of the difficulties of the towed decelerator were circumvented by supporting the aerodynamic surface on a rigid framework in front of the vehicle. This concept, while showing considerable promise, suffered from the weight penalty associated with carrying the structural loads in bending, over large spans.

A second, more recent development of this type is the "tension structure" which has been suggested by Roberts (Reference 5) and Anderson (Reference 6). This system is proposed as a solution to the problem of exploring the tenuous atmosphere of Mars, under conditions in which a typically-dense entry vehicle would impact on the surface before terminal conditions were reached. The decelerator surface in this system is an axisymmetric tension membrane in the shape of a flared cone, which is stretched between the nose of the payload and a large compression ring at the periphery. The retarding force is carried to the payload by pure tension in the aerodynamic surface, so the struc-

tural weight of this element can be very small. This approach therefore appears likely to produce a low- $W/C_D A$ decelerator at a competitive weight fraction.

It is the intention of this report to present another development in the low-wing-loading decelerator field. The basic idea behind this development, which was first proposed by Schuerch and MacNeal (Reference 7), is that it might be feasible to make extremely large decelerator surface areas with low total weight by using a thin membrane which is stiffened by a high spin rate. The Rotornet decelerator design which has grown out of this concept is in many respects similar to the "tension structure" design, the major differences arising from the use of centrifugal inertial forces, rather than structure, to provide radial stiffness. Because the structural loads are resisted by a uniformly distributed tension in the membrane, the surface can be made large enough to permit radiation cooling with low structural weight.

At present the Rotornet concept is in a preliminary stage of development. On the basis of the work which has been done, however, it is possible to state that the concept is sufficiently interesting to warrant further development. In view of this, the purpose of this report is as follows:

- (1) To discuss the factors which affect the design of a rotary hypersonic decelerator,
- (2) To present preliminary-design information which can be used to study trends and to establish the approximate size and weight of the decelerator in terms of the mission parameters,
- (3) To discuss the potential usefulness of the concept,
- (4) To point out areas where important work remains to be done.

The work reported here was conducted with the financial support of the National Aeronautics and Space Administration.

II. GENERAL DESCRIPTION

The aerodynamic surface which is the basic element of the Rotornet system is a large, lightweight, filamentary disk, mounted at its center to a hub on the nose of the payload, as shown in Figure 1, and maintained in a deployed condition by the centrifugal effects associated with a high spin rate. The disk is constructed with continuous fibers that run in curved paths from hub to rim and back, in an axisymmetric fiber pattern such that the tension throughout the disk is (essentially) uniform under the loading of its own inertia in the centrifugal field. The aerodynamic surface is therefore composed of a bidirectional array of structural fibers under tension.

The texture of the filamentary disk is that of a sleazy fabric with the bias direction coinciding at every point with the radial direction on the disk. Thus the surface can deform locally, through the mechanism of trellis shear, without changes in fiber length and without wrinkling. This geometry allows the spinning disk to deform into a cone, as shown in Figure 2, without gross changes in the stress distribution. Under the aerodynamic loading, the disk "cones back", and the load is transmitted to the hub in the form of an axial component of fiber tension. For the Rotornet systems under consideration here this coning back is limited by heating considerations (for this study) to a coning angle of about 30° (cone half-angle of 60°), since it is essential to maintain the detached shock system characteristic of blunt bodies.

Around the periphery of the disk are attached a number of small tip weights, with an aggregate mass of perhaps twenty percent of the mass of the disk. These tip weights serve to improve the behavior of the fabric disk during deployment and in operation at lower altitudes.

They may (for missions requiring gliding and maneuvering) have the form of aerodynamic vanes to counteract the aerodynamic friction torque of the disk; for the ballistic re-entry mission, however, the Rotornet system can operate on the energy of the initial spin-up, without sustaining torque.

The fibers are attached to the hub at the nose of the payload by a clamp ring having a diameter of perhaps fifteen percent of the disk diameter. The clamp ring is, in turn, attached to the payload. If the payload cannot withstand the spin rate this attachment must be made through a bearing, with the orientation of the payload maintained either by vernier rockets or by a motor drive between the payload and the clamp ring.

The attachment structure and the associated gadgetry are protected from the windstream by an insulated, heat-resistant nose cap. This nose cap must rotate with the disk in order that the space between the nose cap and the disk can be minimized (to form a "smooth" transition) without introducing the danger of interference between the rotating disk and the stationary payload structure.

The rotational inertia of the deployed disk is large compared to that of the payload and therefore the energy for the initial spin-up must be provided by rocket motors. For missions requiring retro-rockets, the spin-up energy can be obtained by mounting the retro-rockets on the rim of the nose cap, canted to produce a reaction torque. For missions not requiring retro-rockets the spin-up may be accomplished with small rocket motors mounted on the rim of the disk. These small rocket motors would be started after the disk is deployed and "stiffened" in rotation at a relatively low spin rate.

The operational sequence of the Rotornet in a ballistic re-entry from orbit is shown in Figure 3. After deployment, spin-up, and ejection from orbit, the vehicle loses altitude. The coning angle gradually increases to a maximum of about 30° , after which it decreases. In typical earth entries without lift capability, low supersonic speeds are attained at altitudes above 200,000 ft, thereby permitting potentially large terminal-glide range.

By providing a means to produce a controlled pitching moment, the Rotornet can be made to operate in non-axial, or lifting flight. This pitching moment can be produced by any one of several methods such as center of gravity shift or vernier rocket motors. This possibility is discussed in more detail in a later section.

III. MECHANICS OF THE FILAMENTARY DISK

The Rotornet is basically a uniform-stress (isotensoid) disk, as described in Reference 8. The fiber geometry of the flat disk, shown in Figure 4, consists of a network of circular-arc fiber paths which intersect the origin. The fiber path curvature is necessary for the uniform-stress condition, and must be maintained, as in a net, by "pinning" the fibers at the intersections. For the Rotornet the disk is truncated in order to provide support for the tip weights. The total mass of the tip weights is approximately equal to the mass of the truncated outer section.

An important characteristic of this geometry is that it has uniform increments of arc length between points of intersection in the fiber pattern. Because of this, the disk can be deformed, without changes in arc length, into a cylinder, whereby the fiber pattern becomes an array of helices (the hub expands and the rim contracts to form the two edges of the cylinder). This deformation is diagrammed in Figure 5. The dimensions of the flat development with a square fiber pattern are given in terms of the disk radius. It should be noted that if the disk is to be fabricated using continuous fibers, without structural seams, it must be fabricated with the topology of a cylinder rather than a strip. Since helices are geodesic paths on cylinders, the helical pattern is a practical one from the manufacturing standpoint.

The properties of the isotensoid disk form a convenient set of reference properties for the Rotornet disk. The weight of an isotensoid disk is readily computed from the geometry in terms of the total cross sectional area of the fibers radiating from the origin and the outside radius of the disk:

$$W_{\text{ref}} = \rho_f g a_f \ell_f = \rho_f g a_f \frac{\pi}{2} R_{\text{ref}} \quad (1)$$

where

W_{ref} = weight of isotensoid disk

ℓ_f = length of fiber from origin to periphery

ρ_f = mass density of fiber

a_f = total structural cross-section area of fiber
radiating from origin

R_{ref} = reference radius: outside radius of isotensoid disk

For the present discussion it will be assumed that the mass of the Rotornet is adequately represented by

$$m_R = \rho_e a_f \frac{\pi}{2} R \quad (2)$$

where

R = outside radius of Rotornet disk, corrected to include
area of tip tabs

ρ_e = "effective density" of fiber

i. e., $\rho_e = \frac{1}{a_f}$ (mass per unit length of fiber plus "matrix")

The parasitic mass of the disk is lumped together with the structural mass in the "effective density" term ρ_e in order to preserve the structural cross-sectional area a_f without introducing the complication of an additional term.

The fiber stress distribution in an isotensoid disk is uniform. The stress, s_{ref} , associated with a spin rate, ω , is given by

$$s_{\text{ref}} = \frac{1}{2} \rho_f (\omega R_{\text{ref}})^2 \quad (3)$$

This is one-half of the stress in a spinning hoop of the same material. For the Rotornet disk the nature of the distribution of fiber stress can be changed by changing the tip masses. It can be demonstrated that if the tip-mass force is greater than that of the truncated fiber it replaces, the stress is higher near the rim, while a smaller tip-mass force gives a lower rim stress. In both cases the stress near the center approaches that of the isotensoid disk. The stress distribution in a typical truncated disk for several sizes of tip mass are shown in Figure 6.

If the spinning disk is loaded and deformed by an axisymmetric distribution of normal forces (e. g., aerodynamic pressure) the tension distribution will not change appreciably, provided the deflections are small compared to the radius. This can be explained on the basis that the stress at the periphery is fixed by the centrifugal-acceleration load of the fiber mass near the periphery, and the stress gradient in the fiber is affected only by forces tangential to the fiber (centrifugal and shear forces), and not by the normal forces, which, by definition, have no tangential component. It should be remembered that the inherent shear compliance of the disk permits it to assume any one of a wide spectrum of shapes, without the wrinkling or buckling which might be expected with a shear-resistant membrane.

It can be seen, then, that the deformed shape of the loaded net depends on the aerodynamic load distribution. The aerodynamic load distribution, however, depends on the details of the shape. Thus the equilibrium shape of the Rotornet, for any given set of conditions, must be obtained simultaneously with the aerodynamic load and the tension distribution.

MacNeal (Reference 9) has obtained a family of solutions for this problem by digital computer, using an iterative technique. The aerodynamic loading for this work was taken to be that of a Newtonian pressure distribution, i. e., a loading for which the local normal-pressure coefficient is given by

$$C_p = 2 \cos^2 \beta \quad (4)$$

The results for a typical set of design parameters are shown in Figures 7 through 9 for various values of the loading parameter. Several coned-up shapes are shown in Figure 7; Figure 8 gives the distribution of local coning angle for these shapes. The tension distributions are shown in Figure 9. These curves represent a Rotornet which is truncated at $\gamma_{\text{tip}} = 70^\circ$ ($R/R_{\text{ref}} = 0.94$), has tip tabs with the same mass per unit area as the net at the truncation radius, which tabs increase the effective radius of the truncated net by five percent. The ratio of tip tab mass to mass of the truncated fiber for this case is 0.44. The loading parameter B is defined as

$$B \triangleq \frac{\rho u^2 \cdot \pi R^2}{\omega^2 R \cdot m_R} \quad (5)$$

It can be seen immediately that the resultant (axial) force exerted by the coned-up Rotornet on the hub is

$$F_b = s_b a_f \sin \beta_b \cos \gamma_b \quad (6)$$

where

β = angle between the plane of rotation and the tangent to the meridian

γ = angle between the meridian and the tangent to fiber

and subscript b denotes conditions at the hub. Since $\cos \gamma_b \cong 1$ for all cases of interest, we shall write this as

$$F_b = s_b a_f \sin \beta_b \quad (7)$$

This relation is diagrammed in Figure 10.

The axial component of force in the coned-up net at the hub is taken to be equal to the total aerodynamic force D_c on the net. It is assumed here that the distributed inertia-loading from axial deceleration of the net mass is negligible; this is equivalent to assuming the mass of the net to be negligible compared to the mass of the payload. Thus, given the tension distribution and the coning angle at the hub, we may immediately compute the drag coefficient of the net under the conditions which produced the given shape. This drag coefficient is, of course, identical to that which would be given by an integration of the Newtonian aerodynamic force distribution over the equilibrium shape; in order to obtain the tension distribution it is necessary to determine the equilibrium shape of the spinning net under the aerodynamic loading. The curve of drag coefficient vs. coning angle at the hub for the case considered here is shown in Figure 11, while Figure 12 gives the relation between hub coning angle and the loading parameter.

IV. AERODYNAMIC HEATING

A. Thermal Equilibrium with Radiative Heat Rejection

The thermal equilibrium of the surface of the radiation-cooled Rotornet is given by

$$\dot{q} = \sigma \epsilon(VF) \tau^4 \quad (8)$$

where

$$\begin{aligned} \dot{q} &= \text{heating rate, Btu/ft}^2 \text{ sec} \\ \sigma &= \text{Stefan-Boltzmann Constant} = \\ &0.475 \times 10^{-12} \text{ Btu/ft}^2 \text{ sec } ^\circ\text{R}^4 \\ \epsilon &= \text{emissivity of surface} \\ VF &= \text{view factor} \\ \tau &= \text{absolute surface temperature, } ^\circ\text{R} \end{aligned}$$

The surface of the disk is heated on the front side, but can radiate from both sides. Allowing for the fact that the back side of the disk will be at a somewhat lower temperature than the front side, (the exact amount depends on construction details, as well as on the conditions) and that the back side, furthermore, is slightly concave, it will be seen that the effective "view factor" is somewhat less than two. For the purposes of this study, the view factor was numerically combined with the emissivity, and the product was given the value

$$\epsilon(VF) = 1.4 \quad (9)$$

It is believed that this is a conservative estimate. The effect of using other values for $\epsilon(VF)$ for the temperature range of interest is shown in Figure 13.

B. Convective Heating

The critical convective heating rate for a shallow cone in hypersonic flow can be estimated by assuming the rim heating to be the same as that for the rim of a flat disk. The heating rate distribution over a flat disk is given in Reference 10, and the heating rate at the stagnation point is found to be 0.56 of the stagnation-point heating rate on a sphere of the same radius.

The heating distributions for several blunt shapes, including the disk, are shown in Figure 14. The heating distribution for the sphere is taken from Reference 11, while the heating distribution for the shallow cone is assumed to be essentially that shown in the figure. Note that the heating rate at the rim of the cone is assumed to be the same as for the disk, i. e., 82% of the heating rate at the stagnation point on a sphere of the same radius: Thus we take

$$\dot{q}(R) = .82 \dot{q}_S(R) \quad (10)$$

This estimate is believed to be conservative.

To compute the heating rate at the stagnation point on a sphere, we may take an approximate formula developed by Lester Lees in Reference 12:

$$\dot{q}_S(R) = 22 \times 10^{-9} \frac{\sqrt{\rho}}{\sqrt{R}} u^3 \frac{\text{Btu}}{\text{ft}^2 \text{ sec}} \quad (11)$$

where ρ = density, slugs/ft³
 R = radius of sphere, ft
 u = flight velocity, ft/sec

Taking 82% of this according to Equation (10) gives for the temperature at the rim of the rotor

$$\sigma \epsilon (VF) \tau^4 = \dot{q} = 18 \times 10^{-9} \frac{\sqrt{\rho}}{\sqrt{R}} u^3 \frac{\text{Btu}}{\text{ft}^2 \text{ sec}} \quad (12)$$

Figure 15 shows heating rates and temperatures computed for a disk and the shallow cone of Figure 14 with the rim temperature set at 1650°F. It can be seen that the temperatures are relatively insensitive to the size of uncertainties which are of concern here.

This estimate of heating rate requires that the shock be detached. According to Reference 14, the condition for shock detachment on a sphere-capped cone in hypersonic flight is that the "coning angle" β must be less than about 33 degrees. This consideration limits the maximum coning angle during the critical portion of the trajectory. In this study the maximum allowable coning angle will be arbitrarily taken to be 30 degrees.

The heating in the case of sphere-capped cones with higher coning angles, where the shock is attached, is more severe until the coning angle increases to about 60°. In this case the critical heating occurs near the hub. For the Rotornet such high coning angles are in principle possible, but the overall performance suffers because of the drastic decrease in drag coefficient. There are also associated difficulties having to do with stability. For these reasons this operating regime will not be considered here.

C. Radiation Heating

Radiation heating has been found to be very small compared to convective heating for those cases which could be considered to be of immediate practical interest (manned entry into earth atmosphere with escape velocity or less), when computed according to the estimates of

Lees (Reference 12), or the Handbook of Astronautical Engineering (Reference 13). It can be readily shown that the radiant heating rate at any point in the trajectory, (say, the point of maximum convective heating rate) varies as $1/R^2$, since $\dot{q}_{\text{rad}} \sim \rho^{1.5} R$ (Ref 13), and $\rho \sim 1/R^2$ at the critical point for a given set of entry conditions. Thus the low- $W/C_D A$ vehicle, in spite of the increased shock layer thickness, experiences much lower radiant heating rates. By comparison, the convective heating rate varies as $1/R^{1.5}$.

For entry at hyperbolic velocities the altitudes and densities of interest here lie somewhat outside the range of general interest. Page and Arnold (Reference 14), however, indicate that for altitudes above about 310,000 ft in the earth's atmosphere the radiation heat flux from the shock layer will be limited to about $10 \text{ Btu/ft}^2 \text{ sec}$, independently of the vehicle size. This increment of heat load can be readily absorbed. For hyperbolic entry such a vehicle would almost certainly require maneuvering capability, and the maneuvering altitude would from all indications be considerably above 310,000 ft. Thus, while the picture is far from complete, it appears that, at least for manned earth entry, the radiation heat load will not be overwhelming. For entry into other planets, where the atmospheric composition is different, radiation heating may become more important.

D. Effect of Porosity

Another problem area in which more work must be done is that of determining the effect of porosity on the convective heating rate to a porous fabric cone. It is apparent that if the cool boundary layer is allowed to bleed through the wall there will be some increase in heating. This problem has been examined by Coplan and Freeston (Reference 15) on a theoretical basis, but, as they point out, careful experimental work

needs to be done. Their theoretical work indicates that considerable increase of heating rates may result even from relatively low porosities. While the general conclusions of this study would not be changed drastically even if the heating rates were doubled, still this effect must be carefully considered. Some considerable work has been done (Reference 24) on the development of coatings to reduce porosity in lightweight metallic fabrics, and it seems probable that that technology could be used here. This is one of the major problem areas to be faced in future development work.

V. ENTRY TRAJECTORY STUDIES

In order to study the behavior of the Rotornet as a decelerator for entry into a planetary atmosphere, a digital-computer program was written to make a point-by-point integration of the motion following a given set of initial conditions. The dynamic model used is that of entry into the atmosphere of a round, non-rotating planet, as shown in Figure 16, with vehicle motion restricted to a given diametral plane. The equations of motion which are solved numerically are

$$\frac{du}{dt} = g \sin \theta - \frac{D}{m} \quad (13)$$

and

$$\frac{d\theta}{dt} = \cos \theta \left(\frac{g}{u} - \frac{u}{r} \right) \quad (14)$$

where the symbols are defined as shown in Figure 16. Note that

$$D = D(\rho, u, \beta)$$

since the drag coefficient at any time depends on the cone geometry, i. e., β . Also note that

$$\rho = \rho(h)$$

where h is determined from

$$\frac{dh}{dt} = -u \sin \theta \quad (15)$$

For the function $\rho(h)$, the "U.S. Standard Atmosphere, 1962", Reference 16, was used for Earth, while the "NASA Engineering Models", Reference 17, was used for Mars.

In order to perform any given step of the forward integration process indicated by Equations (13) and (14), it is necessary first to establish the geometry of the net at that particular point. For the purposes of this study we may adopt, as a "standard", a representative set of net parameters, so that the coned-up shape, and therefore the drag coefficient, may be defined in terms of a single variable which is characteristic of the deflected shape. It is convenient to take β_b , the coning angle at the hub, for this characteristic variable. The "standard net" used here will be the one which was used as the example in Section III.

It will be seen that β_b has the nature of a free parameter at every point in the trajectory; we may (in principle) assign any functional form whatever to β_b without altering the basic character of the trajectory. For the preliminary design problem it is of interest to consider whether there is an "optimum" function for β_b , since it is desirable to be able to compare the performance of a decelerator in any given trajectory with its performance in the "most favorable" trajectory having the same initial conditions.

From Equation (12) it is clear that the heating rate \dot{q} for a given velocity decreases as altitude increases. Therefore a radiation-cooled decelerator will experience a lower peak temperature if it can lose velocity at greater altitude; i. e., it should operate continuously at the highest possible drag. High drag is obtained by operating at a (relatively) high spin rate (and therefore high stress), to make the disk relatively "stiff" compared to the aerodynamic load. It is apparent, however, that high drag must not be obtained at the risk of structural failure. The optimum program, then, is to operate with the highest drag coefficient consistent with the predetermined structural limitations. More specifically, this means that for a given set of rotor parameters and initial

conditions, the optimum trajectory is obtained when β_b is programmed to coincide with a constant margin of safety for the hub stress s_b .

Given the basis for the optimum trajectory for a given set of initial conditions, one can examine the manner in which the rotor parameters influence the ability of the decelerator to survive the entry. Note that with the constant, predetermined margin of safety, any decelerator which survives a trajectory is as "safe" as any other (it will be shown that peak deceleration is essentially independent of rotor parameters). Thus the "performance" of a rotor is established by its mass, and the optimum design problem reduces to that of finding the lightest Rotornet which can survive an entry with a given payload mass and given initial conditions. The condition for survival which is of interest here is that the detached shock is maintained throughout the critical portion of the trajectory; i. e., the coning angle at the hub must not exceed the critical value, about 30° .

In order to determine the coning angle program under which the rotor operates at constant safety margin, we may expand Equation (7), which gives the axial equilibrium at the hub (see Figure 10), to include effects of temperature on the allowable stress and the effect of coning angle on the drag force. Thus, Equation (7) may be written

$$s_w(\tau) = s_b = \frac{D_c}{a_f \sin \beta_b} \quad (16)$$

where s_w , the allowable working stress is given by

$$s_w(\tau) = s_{ult}(\tau) \frac{1}{1 + M.S.}$$

By Equation (16), we require that the hub stress s_b be established at a value determined by the temperature. Approximate relations for the ultimate stress, as a function of temperature, for several candidate materials, are given in Section VIII.

The aerodynamic drag force, D_c , on the coned-up net is given by

$$D_c = \frac{1}{2} \rho u^2 \cdot \pi R^2 \cdot C_D(\beta_b) \quad (17)$$

where the drag coefficient C_D (which is based on the area of the flat disk) is shown in Figure 11 as a function of β_b . With these substitutions Equation (16) becomes

$$s_w(\tau) = \frac{\rho u^2 \cdot \pi R^2 \cdot C_D(\beta_b)}{2 a_f \sin \beta_b} \quad (18)$$

This relation can be solved (numerically) for β_b at each point in the trajectory by (1) finding the temperature from the given conditions (ρ , u) by Equation (12), and then (2) finding the working stress $s_w(\tau)$ at that temperature from the strength vs. temperature characteristics of the material. Having solved for the value of β_b which gives the constant safety margin condition, we can compute the cone drag force, D_C . The drag of the nose cap can be neglected for the purposes of this study. We therefore take

$$D(\rho, u, \beta) = D_C \quad (19)$$

for the integration of the equations of motion.

It can be seen from Equations (13) and (16) that by this model the deceleration load of the entire vehicle (payload plus rotor) must be carried by the tension in the fibers at the hub. This model is consistent with that used to compute the net shape (axial-direction body forces were neglected). It is essentially correct for small rotor weight fractions and conservative where the rotor weight is not negligibly small.

The computer results for a typical constant-safety-margin trajectory are shown in Figure 17. This trajectory represents a 2000-lb vehicle with a W/A of 1 lb/ft^2 . The stress vs. temperature function used was that shown in Figure 31 for X-37B glass fiber, which has a zero-strength temperature of 1500°F . It can be seen that the peak temperature occurs at 265,000 ft and the peak deceleration (19 g's) occurs at 243,000 ft. The coning angle peaks at 33° between the temperature and deceleration peaks. Note that θ is essentially constant up to the time of maximum deceleration.

Approximately fifty constant-margin trajectories were run, covering a wide range of initial conditions and vehicle parameters. A comparison of the results of these trajectories showed that the velocity and temperature profiles are essentially independent of the strength vs. temperature characteristics of the structural material of the rotor, provided the coning angle stays within bounds. The coning angle profile, however, is strongly dependent on the material characteristics; if the maximum temperature is close to the maximum allowable for the material, the coning angle will be large, while for a relatively "cool" trajectory the coning angle remains small.

The conclusion to be drawn here is that, at least for preliminary studies, the complicating effects of drag modulation may be safely neglected. For the present purposes, then, we may make use of the body

of "classical" work (for example, Reference 19) which has been done on the idealized entry trajectory, assuming an exponential atmosphere, constant flight-path angle θ , constant drag coefficient C_D , and neglecting the effects of gravity and planet curvature.

A measure of the effect of disregarding changes in the drag coefficient may be seen from Figure 18, which is a plot of maximum temperature vs. the parameter $\pi R^3 C_D / W \sin \theta$. This parameter appears in the solution for maximum stagnation-point heating rate for an idealized trajectory. It was found that the results from trajectories with a wide range of initial conditions and vehicle parameters can be plotted along these curves with very little scatter ($\pm 10^\circ\text{F}$) provided the peak coning angle is less than about 35° . For this plot C_D was taken to be 1.75.

The values for the various other important quantities in the trajectory can also be predicted accurately. Predicted values for maximum deceleration, deceleration at maximum heating, and velocities at these points are, in general, in agreement within a few percent of the computer results, provided that the scale height for the exponential atmosphere model is chosen judiciously ($h_s \cong 18000$ ft for cases in which maximum deceleration and maximum heating rate occur between 250,000 and 300,000 ft). The trajectory flight-path angle is constant within a few percent, up to and including the critical portion of the trajectory, for trajectory angles of 5° or more. For 1° entry angle it was found that the maximum temperature could be predicted using an "effective" entry angle of 1.3° .

Table 1 gives a comparison of various results obtained for the trajectory of Figure 17 both by digital computation and by the exponential atmosphere solutions. The formulas used for the latter are given in

Section VII. Note that the largest error occurs in establishing the point of maximum deceleration. At this stage of the trajectory the slope angle θ is beginning to change rapidly; this has the effect of shifting the time at which the deceleration peak occurs, without changing the peak value appreciably. If the comparison is made at the point in the computer trajectory at which the temperature has the value predicted by the idealized solution (here 1120°F) for the point of maximum deceleration, we find the decelerations and velocities to be in close agreement.

Table 1

COMPARISON OF RESULTS FOR BALLISTIC ENTRY

$$\begin{array}{ll}
 W = 2000 \text{ lb} & u_i = 26,000 \text{ ft/sec} \\
 A = 2000 \text{ ft}^2 & \theta_i = 5^\circ \\
 C_D = 1.75 & h_s = 18,000 \text{ ft}
 \end{array}$$

QUANTITY	COMPUTER TRAJECTORY	IDEALIZED SOLUTION
max. temp, °F	1308	1310
velocity at max. temp, ft/sec	21,500	22,000
deceleration at max. temp., g's	11.9	12.2
max. deceleration, g's	18.7	18.7
temp. at max. decel, °F	1065	1120
velocity at max. decel, ft/sec	14,700	15,800
velocity at $\tau = 1120^\circ\text{F}$	15,600	15,800
deceleration at $\tau = 1120^\circ\text{F}$	18.5	18.7

VI. TORQUE AND SPEED CONTROL

It is essential to the efficiency and reliability of the Rotornet system for the rotation speed of the rotor (if it is not controllable) to be at least predictable within reasonably narrow limits. At present there is not enough known about the aerodynamics of the Rotornet to satisfy this requirement. It is possible, however, to make an estimate of the rotational behavior for a typical case in order to shed light on the gross characteristics.

It is expected that, in maturing, the Rotornet concept would eventually produce a method whereby the rotation speed could be controlled during flight by using as an energy source the hypersonic windstream. At this time, however, it is believed that the early versions should be operable with a minimum of refinement of this type. For this reason the preliminary work has been directed toward establishing the feasibility of operation without speed control or sustaining torque.

The constant-safety-margin trajectory discussed in the previous section assumes that the desired rotation speed is given at each point in the trajectory. From Figure 17b it is seen that this requires that ω first decrease to a minimum value at about the time of maximum temperature, and then increase. To realize such a program for ω would probably require complication and weight far in excess of the penalty of accepting a less efficient spin rate program. It is of interest, therefore, to compute the spin rate and coning angle functions for this trajectory assuming no driving torque, but taking into account an estimate of the aerodynamic friction torque. It will be assumed that the trajectory itself remains unchanged by the changes in coning angle.

To consider the problem of no-driving-torque operation, it is necessary first to write the equation of motion for a rotating cone with a variable coning angle. In the absence of friction torque, the spin rate of the cone changes in order to conserve angular momentum, H , as the coning angle varies. With an applied torque T the spin rate ω is determined by

$$T = \frac{dH}{dt} = \frac{d}{dt} (I\omega) = I_c \dot{\omega} + \omega \dot{I}_c,$$

or

$$\dot{\omega} + \omega \frac{\dot{I}_c}{I_c} - \frac{T}{I_c} = 0 \quad (20)$$

where I_c is the moment of inertia of the coned-up rotor. It can be shown that the moment of inertia for an isotensoid disk is exactly the same as that for a disk of the same mass with uniform mass distribution. Thus we take for the flat Rotornet

$$I = \frac{1}{2} m_R R^2 \quad (21)$$

The moment of inertia for the coned-up Rotornet can also be approximated by

$$I_c = \frac{1}{2} m_R R_c^2 = I \left(\frac{R_c}{R} \right)^2 \quad (22)$$

The rate of change of I_c is

$$\dot{I}_c = m_R R_c \dot{R}_c,$$

so that

$$\frac{\dot{I}_c}{I_c} = 2 \frac{\dot{R}_c}{R_c} = 2 \frac{\dot{R}_c/R}{R_c/R} \quad (23)$$

Note that R_c/R is directly related to β_b by the net characteristics.

The friction torque T is difficult to compute accurately, even for a given cone shape and surface characteristics. For the purposes of an estimate we can assume the torque to be the disk friction torque for the case of subsonic flow toward a rotating disk, noting that the flow behind the normal shock is subsonic. For the fluid properties we take the properties behind the shock. Given this model, the friction torque due to the velocity gradient in the boundary layer can be shown to be

$$T_F = - C_F \frac{\rho}{2} (\omega R)^2 \cdot \pi R^3 \quad (24)$$

where

$$C_F = 0.413 \cdot \frac{1}{\omega R} \sqrt{\frac{u\mu}{\rho R}} \quad (\text{Reference 18}) \quad (25)$$

u = fluid velocity (after shock) ft/sec

ρ = fluid density (after shock) slugs/ft³

μ = viscosity in boundary layer lb sec/ft²

Then

$$T_F = - \frac{\pi}{2} (0.413) R^3 \omega \sqrt{\rho u \mu R} \quad (26)$$

Note that $\rho u = \rho_\infty u_\infty$ for the normal shock. The one remaining property, viscosity, may be taken from the Handbook of Astronautical Engineering (Reference 13), where it is given as a function of temperature. We use an "average" temperature in order to approximate the conditions near the cold wall: $\tau_{\text{avg}} \cong \frac{1}{2} (\tau_{\text{stagnation}} + \tau_{\text{wall}})$. The stagnation temperature is given in the handbook as a function of flight conditions (ρ , u).

The integration indicated in Equation (20) can therefore be performed using Equations (23) and (26). Figure 19 shows the spin-rate and coning-angle programs for the constant margin trajectory of Figure 17 along with

the "corrected" programs. The latter were obtained by starting with the constant-margin spin rate at the point of maximum temperature and integrating in both directions using Equation (20), with flight conditions taken from Figure 17. For this particular case the coning angle peak is above the allowable limit. This indicates that this rotor (which was just barely "safe" in the constant margin trajectory) is too light for the no-driving-torque trajectory. The rotor weight assumed for these calculations was 60 lb, or three percent of the payload weight.

For a porous disk, the momentum drag of the flow through the disk will contribute to the friction torque. Since the porosity must be low for reasons of heating, however, this momentum torque can be expected to be small.

VII. PERFORMANCE RELATIONS

A. General Relations for Rotornet Performance

In Section V it was shown that the results for typical ballistic trajectories can be predicted on the basis of the body of classical, idealized trajectory work such as that done by Allen and Eggers (Reference 19). In this section it will be shown that by combining the results of the classical trajectory analysis with several fundamental relations describing the Rotornet, we can arrive at equations for the rotor size and weight in terms of the mission parameters and material characteristics.

The principal results of the classical solutions for the ballistic trajectory which are of interest to the Rotornet problem are (1) the determination of maximum deceleration, with the conditions (ρ, u) at the point of maximum deceleration, and (2) the determination of the maximum stagnation-point heating rate, along with the appropriate (ρ, u) . These quantities are expressed in terms of entry conditions (u_i, θ_i) and atmospheric scale height, h_s . With a small amount of algebraic manipulation we may re-express these quantities in terms more directly applicable here: entry velocity, u_i , and maximum deceleration, in earth g's (i. e., maximum load factor N_N). We may also determine the deceleration at the point of maximum heating rate, and the heating rate at the point of maximum deceleration. Finally, we may evaluate the equilibrium temperature at maximum deceleration in terms of the maximum temperature.

The various relations are given in the table below. The supporting equations required for their derivation are simply

$$\dot{q} = K \sqrt{\frac{\rho}{R}} u^3, \quad (27)$$

where K is given numerically in Equation (12), and

$$NW = D = \frac{1}{2} \rho u^2 \cdot C_D \cdot \pi R^2 \quad (28)$$

It should be remembered that throughout this work the drag coefficient is considered to be constant.

Table 2

Quantity	(a) max τ	(b) max N
ρ	$\frac{m \sin \theta_i}{3 h_s C_D A}$	$\frac{m \sin \theta_i}{h_s C_D A} \quad (29)$
$\rho = \frac{2NW}{C_D A u^2}$	$\frac{2e N_N W}{3 C_D \pi R^2 u_i^2}$	$\frac{2e N_N W}{C_D \pi R^2 u_i^2} \quad (30)$
u	$\frac{u_i}{e^{1/6}} = .85 u_i$	$\frac{u_i}{e^{1/2}} = .61 u_i \quad (31)$
N	$\frac{e^{2/3}}{3} N_N = .65 N_N$	$N_N = \frac{u_i^2 \sin \theta_i}{2g e h_s} \quad (32)$
$\dot{q}^2 = \frac{1}{k} (\quad)$	$\frac{1}{3} \left(2 K^2 u_i^4 \frac{N_N W}{C_D \pi R^3} \right)$	$\frac{1}{e^2} \left(2 K^2 u_i^4 \frac{N_N W}{C_D \pi R^3} \right) \quad (33)$
τ	τ_T	$\left(\frac{3}{e^2} \right)^{1/8} \tau_T = .89 \tau_T \quad (34)$

The procedure for establishing the performance relation is as follows:

- (1) From the table, set $\dot{q}^2 = (\sigma \epsilon V F \tau^4)^2$, and solve for R:

$$R^3 = \frac{1}{k} \left(\frac{2K^2}{\pi C_D} \right) \frac{u_i^4 N_N W}{(\sigma \epsilon V F \tau^4)^2} \quad (35)$$

- (2) A second relation for R can be developed by combining the relation for axial equilibrium at the hub,

$$s a_f \sin \beta = F_b = N W_P, \quad (36)$$

with the relation for rotor weight

$$W_R = \rho_e g a_f \cdot \frac{\pi}{2} R \quad (37)$$

To avoid double subscripts we shall drop the subscript b when referring to the conditions at the hub; it is to be understood that the performance relations pertain specifically to the hub conditions. Eliminating a_f and solving for R gives

$$R = \frac{2}{\pi} \frac{\lambda \sin \beta}{N} \frac{W_R}{W_P} \quad (38)$$

where

$$\lambda \equiv \frac{s}{\rho_e g} \quad (39)$$

- (3) Equating the two expressions for R and solving for W_R/W_P gives the rotor weight fraction in terms of the various input parameters:

$$\left(\frac{W_R}{W_P}\right)^3 = \left(\frac{\pi}{2}\right)^3 \cdot \frac{1}{k} \left(\frac{2K^2}{\pi C_D}\right) \frac{u_i^4 N_N W}{(\sigma \epsilon V F \tau^4)^2} \cdot \left(\frac{N}{\lambda \sin \beta}\right)^3 \quad (40)$$

This is the desired performance equation. In applying Equation (40), we must use for (k, N, λ, β) values which are appropriate to the condition in question.

B. Performance for Ballistic Entry With Constant Margin of Safety

To establish the performance equation for constant-safety-margin ballistic trajectory, it is unimportant which condition is chosen for evaluating Equation (40); since the safety margin is invariant there is no preferred critical designing condition. It is important however to insure that the maximum value of coning angle β does not exceed the allowed 33° . Since the coning angle profile depends on the material characteristics, the conditions at the point of maximum β are not easily specified in a general way. Given a set of material properties and initial conditions, a coning angle profile with the desired maximum value can be established. The present purpose is served more directly, however, by noting that, for the materials and conditions considered in the trajectory studies, β_{\max} has about the right value when $\beta_T \cong 25^\circ$.

The performance relation for the constant-safety-margin trajectory can therefore be given in terms of the maximum temperature conditions by making the proper substitutions into Equation (40) (taking k and N from column (a) of Table 2).

$$\frac{W_R}{W_P} = \frac{.65 \pi}{2 \sin 25^\circ} \left(\frac{2K^2}{3 C_D \pi} \right)^{1/3} \frac{u_i^{4/3} N_N^{4/3} W^{1/3}}{(\sigma \epsilon V F \tau_T^4)^{2/3} \lambda_T} \quad (41)$$

If we take $C_D = 1.75$, $\epsilon(VF) = 1.4$, and K from Equation (27), and then combine the numerical constants, we obtain

$$\frac{W_R}{W_P} = 6.5 \times 10^{-6} \frac{u_i^{4/3} N_N^{4/3} W^{1/3}}{(\sigma \tau_T^4)^{2/3} \lambda_T} \quad (42)$$

where the following units must be observed:

$$\begin{aligned} u & \text{ ft/sec} \\ W & \text{ lb} \\ \sigma \tau^4 & \text{ Btu/ft}^2 \text{ sec} \\ \lambda & \text{ ft} \end{aligned}$$

The radius R for the constant-margin condition is

$$R = \frac{2 \sin 25^\circ}{.65 \pi} \cdot \frac{\lambda_T}{N_N} \cdot \frac{W_R}{W_P} \quad (43)$$

or

$$R = \left(\frac{2K^2}{3C_D \pi} \right)^{1/3} \frac{u_i^{4/3} N_N^{1/3} W^{1/3}}{(\sigma \epsilon V F \tau_T^4)^{2/3}} \quad (44)$$

Numerically,

$$R = 2.8 \times 10^{-6} \frac{u_i^{4/3} N_N^{1/3} W^{1/3}}{(\sigma \tau_T^4)^{2/3}} \quad (45)$$

Equation (41) shows that the high-temperature characteristics of the structural material affect the rotor weight fraction only through the term $[\sigma\epsilon(VF)\tau^4]^{2/3}\lambda$. It is clear that the lowest weight fraction for a given material is obtained by choosing the maximum temperature τ so as to coincide with the maximum value of this parameter. It is also clear that this temperature-weight parameter forms the basis for comparing materials of different strength/temperature characteristics. This property is discussed in more detail in the section on materials.

The influence of the mission parameters on the rotor weight fraction [Equation (41)] and the radius [Equation (44)] is shown in Figures 20 and 21. The material assumed here is silica fiber, as shown in Figure 31 with a safety factor of 5. The 46,000 ft/sec curves represent conditions that lie somewhat outside the assumptions on which these curves were based, since radiation heating has been disregarded. Furthermore, a 20-g entry would not be a constant- θ path unless the vehicle had lift capability, in which case a less severe trajectory could be flown.

The curves shown in Figures 22, 23, 24 show Equations (41) and (44) specialized for a vehicle weight of 10,000 lb. The curves of thickness represent the thinnest portion of the disk, assuming the disk to be constructed of circular-cross section fibers with "square" packing and without matrix material. This quantity can be determined from the rotor weight and radius by noting that, for the cylindrical development of the disk,

$$W_R = \rho_f g t_e A_{cyl} \quad (46)$$

where t_e is the effective (solid) thickness and A_{cyl} , the area of the cylinder, is

$$A_{\text{cyl}} = \frac{\pi}{2} \cdot \pi R^2 \quad (47)$$

For square packing of round fibers, the material thickness is

$$t_{\text{sq}} = \frac{4}{\pi} w_e$$

Thus

$$t_{\text{sq}} = \frac{8}{\pi^2 \rho_f g} \cdot \frac{W_R}{\pi R^2} \quad (48)$$

If this expression is evaluated for silica fiber ($\rho_f g = .080 \text{ lb/in}^3$) it yields

$$t_{\text{sq}} = 0.070 \left(\frac{W_R}{\pi R^2} \right) \text{ inch} \quad (49)$$

where $W_R / \pi R^2$ is evaluated in units of lb/ft^2 . The thickness of the fabric disk in its square-weave cylindrical development is the same as that of the thinnest portion of the disk, where the weave is square. For the sake of comparison, the thickness of Style 181 glass-fiber cloth based on the same assumptions, is 6.0 mils.

Figures 25 through 28 show the performance characteristics for Rotornet design using Rene' 41, with a safety factor of 2.5. It can be seen that the weight fractions for this material are about three times as great as for silica (even for the lower safety factor), while the rotor thickness, under comparable conditions, remains about the same. The rotor radius is, of course, independent of material characteristics, as shown by Equation (44).

C. Performance for Ballistic Entry
With Constant Fiber Stress

It is of interest to compare the performance of the Rotornet operating under the optimum conditions (constant-margin) with the performance for some other operating condition which might arise. For a meaningful example we may consider the case of constant fiber-stress at the hub, which implies (essentially) constant tip-speed.

To establish the performance equation for the constant-hub-stress case, we must enforce two conditions: (1) we must insure that the rotor has an adequate margin of safety at the point of maximum temperature (which is the point of minimum allowable fiber stress); and (2) we must insure that the coning angle does not exceed the predetermined safe limit (say 30°) at the point of maximum coning, which (for a fixed drag coefficient) corresponds to the point of maximum dynamic pressure, or maximum deceleration.

To establish a safe working stress at maximum temperature, we write the performance equation in terms of the conditions at maximum heating:

$$\left(\frac{W_R}{W_P}\right)^3 = \left(\frac{\pi}{2}\right)^3 \left(\frac{2K^2}{3\pi C_D}\right) \frac{u_i^4 N_N W}{(\sigma \epsilon V F \tau^4)^2} \left(\frac{N_\tau}{\lambda_\tau \sin \beta_\tau}\right)^3 \quad (50)$$

To determine β_τ in terms of $\beta_N = 30^\circ$, note that the two conditions must give compatible results for R and W_R/W_P . Thus, from Equation (38)

$$\frac{(\pi/2) R}{W_R/W_P} = \frac{\lambda_\tau \sin \beta_\tau}{N_\tau} = \frac{\lambda_N \sin \beta_N}{N_N}$$

For constant stress, $\lambda_\tau = \lambda_N = \lambda$. We may therefore substitute

$$\frac{N_N}{\lambda \sin \beta_N} = \frac{N_\tau}{\lambda \sin \beta_\tau} \quad (51)$$

in Equation (50). This gives the desired performance equation for constant-stress operation:

$$\frac{W_P}{W_R} = \frac{\pi}{2 \sin \beta_N} \left(\frac{2K^2}{3\pi C_D} \right)^{1/3} \frac{u_i^{4/3} N_N^{4/3} W^{1/3}}{(\sigma \epsilon V F \tau^4)^{2/3} \lambda_\tau} \quad (52)$$

where $\beta_N = 30^\circ$.

The coning angle at maximum temperature is given by

$$\sin \beta_\tau = \frac{N_\tau}{N_N} \sin \beta_N = 0.65 \sin \beta_N \quad (53)$$

For $\beta_N = 30^\circ$, $\beta_\tau = 19^\circ$. The minimum weight design for constant-stress operation is obtained, as in the constant-margin case, by choosing τ_τ to coincide with the maximum value of $(\sigma \epsilon V F \tau^4)^{2/3} \lambda$.

Comparing the weight fraction given by Equation (52) with that for the constant-margin condition [Equation (41)] we see that

$$\frac{(W_R/W_P)_S}{(W_R/W_P)_M} = \frac{(\sin \beta_\tau)_M}{(.65 \sin \beta_N)_S} = \frac{\sin 25^\circ}{.65 \sin 30^\circ} = 1.30$$

This shows that the weight penalty for operating at constant hub stress instead of constant safety margin is 30%.

Since the hub stress is closely related to the tip speed, the constant-stress condition closely approximates constant tip speed. If the rotor operates without sustaining torque the angular momentum will decrease in the interval between maximum temperature and maximum deceleration. Since the coning angle increases during that interval, however, the rotational moment of inertia decreases, tending to increase the tip speed. The intricacies of these relationships have not yet been carefully explored, but it appears that there is in general a net increase in tip speed between the times of maximum heating and maximum deceleration, even though the angular momentum continuously decreases. If this is the case then the rotor weight fraction would be somewhat closer to the constant-margin minimum than that computed for constant-stress operation.

D. Performance for Steady-State Equilibrium Glide

Another case which is of considerable interest insofar as the potential usefulness of the Rotornet is concerned is that of equilibrium glide at superorbital velocity. The performance equations for this case can be established readily from the work done previously.

From the trajectory equations it can be seen that a vehicle traveling at a velocity of

$$u = \sqrt{ng r} = \sqrt{n} U ,$$

where

$$U = \sqrt{rg} \cong 26,000 \text{ ft/sec}$$

under conditions in which the rate of change of θ can be neglected, requires a lift force of

$$L = mg(1-n) \tag{54}$$

to maintain the glide path. This condition is diagrammed in Figure 29. If the lift force is a small, fixed fraction of the drag, then

$$\frac{L}{D} = \frac{1-n}{N} \quad (55)$$

where N is the load factor in the direction of the flight path. Note that a higher L/D allows operation with a lower N .

We can now arrange the parameters of the design problem to allow the rotor radius and the glide path altitude to be chosen so as to match the allowable temperature and load factor. As before, the heating and drag relations, Equation (27) and (28), can be combined to yield expressions for the various quantities in terms of C_D and N . If we replace N with L/D according to Equation (55) we obtain for the heating rate

$$\dot{q}^2 = 2K^2 \left[\frac{NW}{C_D \pi R^3} \right] u^4 = 2K^2 \left[\frac{(1-n)W}{C_L \pi R^3} \right] n^2 U^4 \quad (56)$$

where

$$C_L = C_D \cdot \frac{L}{D} \neq 0$$

The expressions for R^3 for this case can be obtained from Equations (56) and (38)

$$R^3 = \frac{2K^2}{\pi C_D} \cdot \frac{W U^4}{(\sigma \epsilon V F \tau^4)^2} \cdot \frac{n^2(1-n)}{L/D} = \left(\frac{2}{\pi}\right)^3 \left(\frac{\lambda \sin \beta}{N}\right)^3 \left(\frac{W_R}{W_P}\right)^3 \quad (57)$$

Note that these relations are valid only for $\frac{L}{D} \ll 1$.

Solving for W_R/W_P here gives

$$\frac{W_R}{W_P} = \frac{\pi}{2} \left(\frac{2K^2}{\pi C_D} \right)^{1/3} \frac{W^{1/3} U^{4/3}}{(\sigma \epsilon V F \tau^4)^{2/3} \lambda} \cdot \frac{n^{2/3}}{\sin \beta} \left(\frac{1-n}{L/D} \right)^{4/3} \quad (58)$$

where

$$\left(\frac{1-n}{L/D} \right)^{4/3} = N^{4/3}$$

To consider a sample case, take

$$u = 45,000 \text{ ft/sec } (n = 3)$$

$$\tau = 1650^\circ\text{F}$$

$$N = 10 \quad \left(\frac{L}{D} = -0.2 \right)$$

$$W = 4000 \text{ lb.}$$

This gives, from Equations (57) and (28)

$$R = 49 \text{ ft}$$

$$\rho = 3 \times 10^{-9} \text{ slugs/ft}^3 \quad (h = 306,000 \text{ ft})$$

The radiant heating for this example, according to Reference 13, is about 5 Btu/ft²-sec, compared to 13 Btu/ft²-sec for convective heating. This would raise the surface temperature to about 1800°F. The rotor weight fraction for this case is 3.7 percent, using Silica fiber with a safety factor of 5.

E. General Remarks Concerning Performance

It can be seen from the foregoing that the convective heating rate for the Rotornet is determined by a property of the vehicle that is, in

effect, a density rather than a wing loading (which has the nature of a thickness). This is readily shown by rewriting Equation (33):

$$\dot{q} = \sigma \epsilon (VF) \tau^4 = \sqrt{2} K u^2 \left(\frac{NW}{C_D \pi R^3} \right)^{1/2} \quad (59)$$

Here NW is a force, while $C_D \pi R^3$ can be considered a volume; consequently the ratio can be thought of as a "load density". Figure 30 is a plot of the relationship between maximum temperature and the load density. It is apparent that for different-sized vehicles of the same type with the same temperature limitations, the load densities must be the same. The ballistic parameter $W/C_D A$ for such vehicles, however, depends on size.

The load-density parameter for heating during ballistic entry has an equivalent counterpart for entry under equilibrium glide conditions. This parameter is also, in effect, a vehicle density. Eggers (Reference 1) has found that, for a wide range of entry-trajectory problems using constant aerodynamic coefficients, the maximum rate of heat transfer to the stagnation point by convection is proportional to the parameter $(W/C_D AX)^{1/2}$ for ballistic trajectories and to $(W/C_L AX)^{1/2}$ for gliding trajectories, where X corresponds to the Rotornet radius. Thus the conclusions reached concerning the effect of rotor size on maximum temperature appear to be applicable to the general case of entry into an exponential atmosphere.

It should be recognized that the heating rate at the rim of the Rotornet changes with angle of attack. Stainback, in Reference 20, shows distributions for local heat transfer coefficients over the surface of a disk for various angles of attack (the value of K used here for axial flow was derived from these data). From the data in that report, it can

be seen that the heating rate on the up-stream side of a disk pitched 15° from the normal is increased over that of the axial flow case by about ten percent. This would produce a temperature increase of about 50°F for the range of temperature considered here. It is not known how this value is affected by the coning angle of the Rotornet.

For a flat disk in Newtonian flow a 15-degree angle of attack gives an L/D of about 0.25. This value decreases as the coning angle increases. The center of pressure on the face of a disk at an angle of attack of 15 degrees lies about four percent of the radius from the center of the disk, but this value increases with coning angle. The center-of-pressure shift must, of course, be matched by a shift of the center of gravity of the decelerating mass. It appears that one of the principal optimization problems for lifting flight will be that of finding the coning angle which gives the lightest overall system, taking into account the heating increase from the asymmetrical flow and the structural weight associated with the required center of gravity shift.

Another relationship which is important to the understanding of the structural characteristics of the Rotornet can be seen from Equation (38), which can be rewritten as

$$\frac{W_R}{NW_P} = \frac{\pi}{2 \sin \beta} \left(\frac{R}{\lambda} \right) = (\text{geom. const}) \cdot \left(\frac{R}{\lambda} \right) \quad (60)$$

Equation (60) expresses a very fundamental property for this structure: the ratio of structural weight to supported force is proportional to the absolute size of the structure. This "size effect" relation is typical for externally-loaded filamentary structures.

A measure of the effectiveness of the Rotornet as a load-carrying structure is obtained by computing the length of a tension member (a rope)

of the same material as the rotor fibers, having the same weight as the rotor, and capable of carrying the same load with the same safety factor. The length of such a rope would be

$$l = \frac{\pi}{2} R \cdot \frac{1}{\sin \beta}$$

or, for $\beta = 30^\circ$,

$$l = \pi R \tag{61}$$

Thus the Rotornet weight is about the same as the weight of the shroud lines of an equivalent parachute which would be trailed 1.5 diameters behind the payload.

VIII. MATERIALS

It was shown in Section VII that, insofar as the structural requirements of the Rotornet are concerned, the merits of high-temperature structural fibers can be compared on the basis of the temperature-weight parameter $[\sigma\epsilon(VF)\tau^4]^{2/3} \lambda$, where λ is the allowable working stress, at the temperature τ , divided by the weight density. To be strictly correct, a comparison of materials should take into account the non-structural weight associated with protective coatings, binders, etc., that may be required in a useful design.

At this preliminary stage, it is difficult to make a meaningful estimate for this parasitic weight fraction, except to say that, in principle, it can be small: the nature of the disk is such that it must have the shear compliance of uncoated fabric; the fibers are continuous, without structural joints, and are loaded primarily by body forces, so that bulk matrix material is unnecessary; and the operating temperature of the fabric is (as far as can be determined) well above that of any known flexible organic matrix material. It is apparent that one important area in which work must be done is that of developing suitable, efficient coating materials to protect the fibers of high-temperature, flexible, structural fabrics from damage by handling and self-abrasion.

The high-temperature characteristics of the most promising candidate materials are shown in Figures 31 and 32. The ultimate-strength data for the glass and silica fibers were taken from single-fiber tests under laboratory conditions; there appears to be at this time, little chance of achieving such strength in a large structure. René 41, which appears to be the most likely candidate among the metallic fibers, is far inferior to the glasses on the basis of laboratory strength, but the

values shown are much more nearly representative of the strength that might be attained in service. The high-temperature organic fiber, HT-1, would be mechanically ideal for this purpose, but it is far too sensitive to temperature to be useful here.

The temperature-weight parameter is plotted in Figure 32 as $(\sigma \tau^4)^{2/3} \lambda_{ult}$ vs. τ . The peak value of each curve establishes the operating temperature for which the rotor will have the least weight, as is shown by the performance equation. It can be seen, however, that the peaks are relatively flat over a temperature range of about 400° F, so that the rotor weight fraction is not sensitively dependent on peak temperature within this range. This effect is shown in Figures 24 and 28. It is likely that considerations of rotor radius or thickness, or, perhaps, capsule heating, will establish the design at some point other than the maximum value of the temperature-weight parameter.

The effect of emissivity has been disregarded in this comparison because emissivity is primarily a property of the surface, rather than of the structural material; since the fiber surface will probably be covered by a protective coating, the emissivity of the fiber material is not of prime importance here. It will be important, however, to have protective coatings with desired emissivity characteristics: high emissivity at temperatures in the neighborhood of 1600° F, with low absorbtivity for radiation from the shock layer.

IX. VIBRATIONS, DYNAMIC STABILITY AND CONTROL

The effort expended under the present contract on vibrations, dynamic stability and control is reported in detail in References 9 and 25. The analysis of rotor net vibrations, reported in Reference 9, makes use of the large motion analysis of rotor net deflections and stresses described in Section III. The analysis of stability and control, reported in Reference 25, is an independent effort using highly simplified equations of motion. It is hoped that an integrated approach that is applicable in both problem areas and is also applicable to such matters as panel flutter and dynamic loads can be developed in the future.

The starting point taken for the analysis of vibrations is the statically deformed equilibrium shape of the rotor net under axisymmetric aerodynamic loads. Energy methods are used to obtain a mathematical model that describes the small perturbation motions from the equilibrium state. Three types of energy are employed: kinetic energy, elastic strain energy, and work done against static preloads. The third type of energy is worthy of special notice because it is usually ignored in the analysis of structures with great rigidity. It plays a dominant role in the vibration analysis of very flexible structures such as cables, membranes and helicopter rotor blades.

For the special case of a flat rotating net the vibrations in the plane of the net are uncoupled from the vibrations normal to the plane of the net. Typical mode shapes are shown in Figures 33 and 34. For the modes shown in these figures all displacement quantities vary as the sine or cosine of the azimuth angle. Such modes are particularly important because they produce resultant forces and moments on the hub that are reacted by the inertia properties of the payload.

The amount by which the frequency of the first out-of-plane mode exceeds one cycle per revolution in the rotating system is a direct measure of the ability of the Rotornet to exert moments on the hub and thus to influence the stability and control characteristics of the vehicle. Analysis of a flat isotensoid net shows that the frequency of the first out-of-plane mode is, in cycles per revolution,

$$\bar{\omega} = 1 + \frac{1}{\pi} \cdot \frac{b}{R} \quad (62)$$

Thus the hub radius b is an important parameter for the stability and control of Rotornets.

The mode shape for the first in-plane mode, Figure 34, indicates a large shear strain near the hub due to the fact that the fibers approach the center of the disk along nearly radial lines. The frequency of this mode could, presumably, be raised substantially by increasing the fiber angle near the hub.

The main effects of static coning on vibrations are to couple in-plane and out-of-plane vibration mode shapes and to lower the vibration frequencies. These effects are illustrated in Figures 35 and 36 which correspond to Figures 33 and 34 except that the net is axisymmetrically deformed with a coning angle of approximately 30 degrees at the hub (See Figure 7 for static deflection shape). The fact that the frequency of the first flapping mode is below one cycle per revolution is expected to have an important, but as yet unexplored, effect on stability and control characteristics.

In the analysis of flight stability undertaken in the present study, the Rotornet was assumed, a priori, to have certain simple modes of deformation. It was assumed that the statically deformed net has an

exactly conical shape. The types of motion permitted were those in which each generator of the cone rotates as a rigid body about its intersection point with the hub and such that the motions of different generators vary as the sine or cosine of the azimuth angle. In effect the Rotornet was permitted to tilt as a (nearly) rigid body with respect to the hub. Strain energy due to elastic deformation was ignored. The degrees of freedom permitted for the entire vehicle in each of two perpendicular planes were

- (1) Rigid lateral translation of the payload
- (2) Rigid pitch of the payload
- (3) Elastically restrained tilt of the hub with respect to the payload
- (4) Tilt of the Rotornet with respect to the hub as described above.

Motions in the perpendicular planes are coupled by gyroscopic effects of rotation. Thus eight degrees of freedom must be considered simultaneously, leading to a stability polynomial of 16th order. The polynomial was reduced to 8th order by consideration of symmetry at the expense of the introduction of complex coefficients.

Aerodynamic influence coefficients for small motions from static equilibrium were computed using the Newtonian flow concept, i. e., by assuming that the aerodynamic force on a surface is normal to the surface and is proportional to the square of the normal component of relative velocity between the surface and the undisturbed air stream.

The stiffening effects of static forces (static centrifugal force, static aerodynamic force, and steady axial deceleration) were included in the analysis.

Derivation of the complete equations of motion was quite lengthy, indicating that an extension of the approach taken to include more degrees

of freedom is probably not competitive with other approaches.

Solutions were obtained on a digital computer. For the initial investigations flexibility between hub tilt and rigid body pitch of the payload was eliminated. Subsequently, hub tilt was restored as an independent degree of freedom in order to investigate the effects of various stability augmentation devices inserted between the hub and the payload.

Two different types of instability were discovered. The first type is a violent divergence that occurs at high coning angles when the center of gravity of the payload is located off of the hub plane. Stability boundaries for the type of instability in terms of coning angle, height of the center of gravity above the plane of the hub, and hub radius, are shown in Figure 37. It is seen that the deleterious effect of center-of-gravity height may be offset by increased hub radius. The instability has a fairly simple physical explanation. The static longitudinal load on the payload due to deceleration has a destabilizing effect identical to that of static load on a column. The gyroscopic inertia forces on the rotor disc produce a stiffening effect on the hub that is proportional to hub radius. Instability occurs when the former effect overcomes the latter.

The second type of instability that was observed is a mild spiral instability that is common to all helicopter-like devices. In this mode, the vehicle executes a slowly diverging spiral motion accompanied by a slight outward tilt of the vehicle away from the axis of the spiral. Relative motion between the rotor disk and the payload is small. It was discovered that the tendency to instability could be suppressed by means of an attitude reference gyro and an actuator that would tilt the hub relative to the payload in a direction displaced 90° with respect to the error signal from the gyro. The effect of the magnitude and phase of the actuator gain, A , on the stability of the spiral mode is plotted in Figure 38. It

was also discovered that an actuator gain that stabilized the spiral mode also tended to destabilize one of the higher modes of the system. The latter tendency was alleviated by inserting a parallel spring and damping compliance in series with the actuator as indicated in Figure 39.

The investigation of the dynamic stability of the Rotornet must be regarded as being in a very primitive state at the present time. Coupling effects between in-plane and out-of-plane motions of the rotor disk must be included in order to obtain reliable results. No analyses have been made of higher mode instabilities (panel flutter) of the Rotornet, and the investigation of control characteristics has not begun.

X. MECHANICAL DESIGN CONSIDERATIONS

A. Fabrication

The Rotornet disk is a unique structural element in many respects, and, while it is not particularly exotic as aerospace structures go, the equipment necessary to fabricate a full-size disk does not now exist. It is apparent that manufacturing processes must be considered carefully if the Rotornet is to become a useful concept.

It was shown in Figure 5 that the disk can be formed as an array of helices on a cylinder. If the cylinder is flattened, the helical pattern becomes a diagonal pattern on a wide belt. In either case, the fiber paths are geodesic lines; fibers placed along these lines will tend to remain in place, rather than slide laterally as is the case for non-geodesic fiber patterns. For this reason, the "geodesic development" of the disk will probably prove to be the form in which the fiber pattern is established.

It should be recognized that the fiber pattern of the Rotornet disk could be any family of opposing spiral paths. The constant-curvature (circular) pattern of the isotensoid disk seems particularly appropriate at this point because it offers the combination of a desirable stress distribution and a flat (or cylindrical) geodesic development. Other spiral patterns could also be used, and the fabrication could be made in the geodesic development, by starting with a mandrel of some other shape, e.g., a section of a sphere or a cone.

In order to maintain the curvature of the fiber pattern in the flattened spinning disk it is necessary to "pin" the intersections. This can be accomplished by sewing or otherwise fastening together the opposing families of helices; it can also be accomplished by weaving or braiding

the two families together. If the fiber pattern can be satisfactorily pinned without interweaving, then the fiber can be placed on the cylinder using standard techniques for filament winding. Considering the brittle, abrasive character of fibrous glass and silica, however, it is believed that interweaving will be necessary.

The weaving process required here is not readily accomplished on a standard loom because of the width, the diagonal nature of the weave, and the requirement that the belt be continuous. Because of the extremely large number of fiber intersections, it is apparent that if the weaving pattern is to be fine (to give the disk a cloth-like texture), a large, expensive, high-speed machine will be required. An alternative lies in using a "basket weave" with parallel-fiber tapes, perhaps an inch wide. This would reduce the number of intersections by several orders of magnitude and allow fabrication to be completed in several weeks with weaving rates of the order of one intersection per second. A typical basket-weave pattern of parallel fiber tapes is sketched in Figure 40. The upper limit for practicable tape width will probably be determined by the tendency of basket-weaving tapes to bunch as a result of handling, thereby leaving holes in the rotor surface.

Two potentially useful schemes for making a basket-weave disk are shown in Figures 41 and 42. The basket-woven-cylinder approach of Figure 41 is adaptable to fabrication of models and prototypes, since no special machinery is required if fabrication time is not important. For higher production rates this process could be mechanized. A somewhat more easily mechanized scheme is shown in Figure 42 which depicts a basket-woven disk being made in the form of a flat-braid belt. The machinery required here consists basically of a conveyor to support the belt, and a braiding head which provides the means to drive a number of rolls

of tape back and forth across the width of the belt, along a crisscross track. The final portion of such a belt would have to be spliced by another process.

The fibers should be continuous around the tip weights, in order to avoid the problems associated with transferring the tip-mass force through a clamp. A typical Rotornet for a 2000-lb vehicle for manned ballistic entry might have tip weights in the form of clips made from eighth-inch-diameter Rene' 41 rod.

The parallel-fiber tapes, particularly for glass and silica fibers, should be made as special-run stock. In order to preserve as much of the laboratory strength as possible, the glass filaments should be coated immediately after they are formed. The success of the concept for high temperature operation will depend very heavily on the qualities of the protective coating material.

B. Mounting Provisions

The woven disk is attached at its center to a clamp ring with a diameter of about fifteen percent of the rotor diameter. This clamp ring is attached to a hub structure which rotates with the net. The hub structure is protected from the windstream by an insulated, heat-resistant nose cap, as shown schematically in Figure 43. Although this nose cap can reject heat by radiation from one side only, the total heat load is only a few hundred Btu per sq. ft; thus a small amount of thermal capacity will be sufficient to control the temperature.

For manned entry, the hub supports the capsule through a bearing. In order to apply a pitching-moment control to the hub, either for stability or for non-axial flight, the stationary race of the bearing can be

attached to the capsule through a mechanism to tilt the hub with respect to the capsule. Depending on the power requirements, however, the required pitching moment may be obtained more economically by the use of a fixed bearing and vernier rockets mounted on the capsule.

C. Packaging and Deployment

Of the various packaging and deployment schemes which have been considered, the one which appears to be the most promising is to stow the rotor in an annular chamber on the hub near the clamp ring, and to deploy it by spinning the hub. The rotor is packed by wrapping it around the hub in the reverse direction. This can be accomplished by spreading the rotor disk out on a smooth surface around the hub, then rotating the hub in the forward direction, allowing the periphery of the rotor to slide toward the hub as the wrapping progresses.

The deployment can be accomplished by spinning the hub slowly, releasing the rotor, and applying torque to the hub to accelerate the rotor slowly until it is fully deployed. This process is illustrated schematically in Figure 44. After the rotor is deployed and spinning slowly, the final spin-up torque can be applied either by rocket motors mounted on the nose cap or, for larger rotors, with small rocket motors at the periphery.

XI. POSSIBILITIES FOR THE FUTURE

From the operational standpoint, the low- $W/C_D A$, radiation-cooled decelerator differs from the high- $W/C_D A$ decelerator in two major respects: it becomes effective at a higher altitude, and it offers a weight advantage for certain missions. Of the various low- $W/C_D A$ systems which have been proposed, the Rotornet appears to offer (potentially) the greatest weight advantage, at a cost of increased mechanical complexity. If the development of this system is to be undertaken, it must be justifiable on the basis of some firm requirement that cannot satisfactorily be met with existing systems.

One type of mission in which the low- $W/C_D A$ system offers distinct advantages is the exploration of the planetary atmospheres. A "light" vehicle can decelerate at higher altitude and descend more slowly, to allow more time and better conditions for taking measurements and transmitting the data.

One of the first such exploration missions now planned is that of the Mars landing probe, in which a small, instrumented payload is to be placed on the planet surface. A Rotornet design for this mission is shown in Figures 45 and 46. The fore-and-aft symmetry of this particular configuration is suggested as a means to satisfy the requirement for deployment and entry without attitude reference. Note that the payload on this vehicle spins with the rotor. The initial condition for this mission is vertical entry at 25,000 ft/sec. The atmosphere assumed was the most pessimistic (Model 3) given in Reference 17.

The weight advantage of the Rotornet over other systems is greatest for shallow entry such as is required for most manned missions, since ablator weights show a slight decrease with increase of entry angle

(Reference 1), whereas the Rotornet weight increases rapidly with entry angle. Thus the simple inertia-driven disk for ballistic entry at 10 g's shows a potential for important savings in weight compared with the heat shields of such vehicles as Mercury and Gemini. This weight advantage will increase for ballistic entry at higher velocities, provided the maximum deceleration is limited.

For lifting flight, other considerations enter. Rigid airframes capable of gliding flight at hypersonic velocities are considerably heavier than the simple axisymmetric heat shields, and the requirement for thermal protection becomes more severe with small-radius leading edges and extended flight times. For the Rotornet, the introduction of hypersonic lift capability acts to reduce the rotor weight. Allowing for an increase in the capsule structural weight required by the asymmetric loading condition and a general increase of complexity, it appears that total change in the system weight will not be important. A sketch of a vehicle with an offset center of gravity for lifting flight is shown in Figure 47.

It is believed, therefore, that the Rotornet development should be directed toward achieving lift capability. This will allow superorbital entry with relatively large corridors and small weight fractions. The maneuvering capability will also provide large footprints for decreased ground support. The variable-geometry capability of the rotor is well suited for this, since the allowable range of angle of attack and coning angle permits (in principle, at least) operation with high L/D , high C_L , or high C_D .

The Rotornet is potentially inexpensive, if the required quantities can eventually justify the cost of production machinery, since the basic materials are not necessarily expensive and since the weight of material

in each rotor is small. It is doubtful that a given rotor would be used more than once. It is important to note, however, that the vehicle itself should not be damaged during re-entry. The cost of outfitting a vehicle with a new Rotornet for each mission would be small compared with the refurbishing expense required for a rigid lifting vehicle. In this regard the Rotornet is similar to the parachute; eventually the logistics could be similar.

These considerations suggest that for operations requiring a "shuttle service" to and from an orbiting station, a Rotornet system (sufficiently advanced) would provide at least three important features; extremely low airframe weight, high maneuvering capability with large footprints, and low refurbishing cost.

XII. CONCLUSIONS

On the basis of the results of the analytical design study described in this report, it appears that the Rotornet concept is capable of providing a radiation-cooled, low- $W/C_D A$ decelerator system with an extremely low weight fraction. Furthermore, the concept shows an excellent potential for providing maneuvering capability, over the full range of velocities. These factors, together with the potentially-low vehicle cost, combine to make the concept attractive for a wide spectrum of mission parameters, ranging from hyperbolic entry to shuttle service operations.

There are, of course, a number of problems which remain to be solved. Some of these (e.g., effects of porosity) must be approached through experimental research, while others (e.g., stability) can only be investigated through careful theoretical work. Furthermore, since the mechanical characteristics of the structure are new, there must be a certain amount of materials and process development. It is believed, however, that all of these problems are amenable to solution by more-or-less conventional techniques, and that a systematic development program can be expected to yield useful hardware.

It is therefore recommended that development of the Rotornet concept be continued to the point at which re-entry experiments can be made with a full-size rotor.

REFERENCES

1. Eggers, Alfred J., Jr., "The Possibility of a Safe Landing," Space Technology, Part II, Chapter 13, John Wiley & Sons, Inc. 1959.
2. Gazley, Carl, Jr., "Atmospheric Entry", Handbook of Astronautical Engineering, Chapter 10, McGraw-Hill Book Company, First Edition, 1961.
3. Performance of End Design Criteria for Deployable Aerodynamic Decelerators, ASD-TR-61-579, (Also available as DDC AD 429 971), December 1963.
4. Study of a Drag Brake Satellite Recovery System, ASD TR-61-348, January 1962.
5. Roberts, Leonard, "Entry Into Planetary Atmospheres," Astronautics and Aeronautics, pp. 22-29, October 1964.
6. Anderson, Roger A., "Space Technology - 1964." Astronautics and Aeronautics, pp 14-20, December 1964.
7. Schuerch, H. U. and MacNeal, R., Deployable Centrifugally Stabilized Structures for Atmospheric Entry From Space, NASA CR-69, July 1964.
8. Kyser, A. C., The Uniform-Stress Spinning Filamentary Disk, NASA CR-106, May 29, 1964.
9. MacNeal, Richard H., Mechanics of a Coned Rotating Net, Astro Research Corporation, ARC-R-178, Santa Barbara, Calif., January 1965.
10. Stainback, P. Calvin, Pressure and Heat Transfer Measurements on the Flat Face of Blunted 10° Half-Cone Body (Semidisk) at a Mach Number of 6.15, NASA TN D-1628, May 1963.
11. Lees, Lester, "Laminar Heat Transfer of Blunt-Nosed Bodies at Hypersonic Flight Speeds," Jet Propulsion, April 1956.
12. Lees, Lester, "Recovery Dynamics—Heat Transfer at Hypersonic Speeds in a Planetary Atmosphere," Space Technology, Part II, Chapter 12, John Wiley & Sons, Inc., 1959.

13. Hildebrand, R. B., "Aerodynamic Fundamentals," Handbook of Astronautical Engineering, Chapter 5, McGraw-Hill Book Company, 1961.
14. Page, William A. and Arnold, James O., Shock-Layer Radiation of Blunt Bodies at Reentry Velocities, NASA TR R-193, April 1964.
15. Coplan, Myron J. and Freeston, W. Denney, Jr., High Speed Flow and Aerodynamic Heating Behavior of Porous Fibrous Structures, WADD Technical Note 61-58. (Also available as DDC AD 271 960), October 1961.
16. U. S. Standard Atmosphere, 1962.
17. Levin, George M., Evans, Dallas E., and Stevens, Victor (eds), NASA Engineering Models of the Mars Atmosphere for Entry Vehicle Design, NASA TN D-2525, November 1964.
18. Schlichting, H., Boundary Layer Theory, McGraw-Hill Book Company, 1955.
19. Allen, H. Julian and Eggers, A. J., Jr., A Study of the Motion and Aerodynamic Heating of Ballistic Missiles Entering the Earth's Atmosphere at High Supersonic Speeds, NACA TR 1381, 1958.
20. Chu, Chauncey C., Gardella, Joseph W., and Kaswell, Ernest R., Research Leading to Optimum Fibrous Structures of HT-1 Yarn, Technical Documentary Report Number ML TDR 64-78, January 1964.
21. A Comparative Properties Analysis, Owens-Corning Fiberglas Corporation, NY-AD-64-3A, New York, N. Y., September 1964.
22. Otto, W. H., Properties of Glass Fibers at Elevated Temperatures, DDC AD 228 851, August 1959.
23. Johnson, Dennis E., Newton, Emerson H., et al, Metal Filaments for High Temperature Fabrics, ASD Technical Report 62-180 (Also available as DDC AD 276 292), February 1962.
24. West, Phillip, "Metal Fabrics for High Temperatures," Materials in Design Engineering, pp. 102-105, January 1965.
25. MacNeal, R. H., Flight Stability of Rotor Nets, Astro Research Corporation, Report ARC-R-178, Santa Barbara, Calif., February 1965.

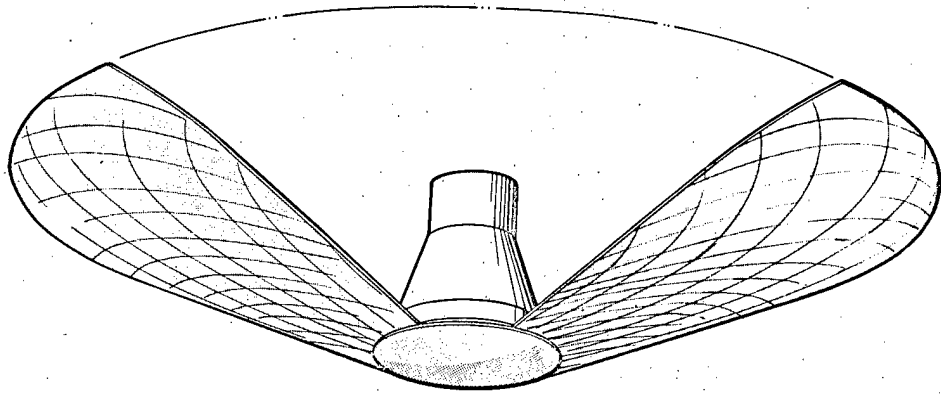


Figure 1. Rotornet Decelerator

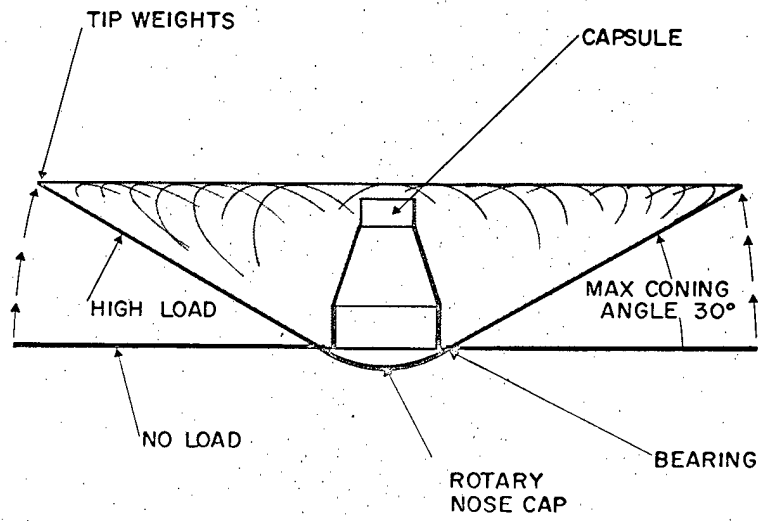


Figure 2. General Arrangement

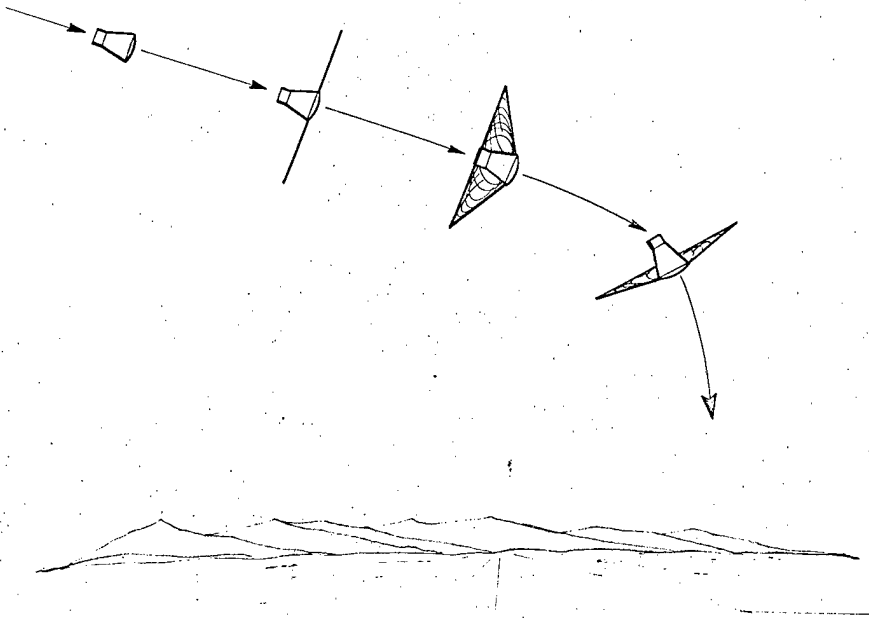


Figure 3. Operational Sequence

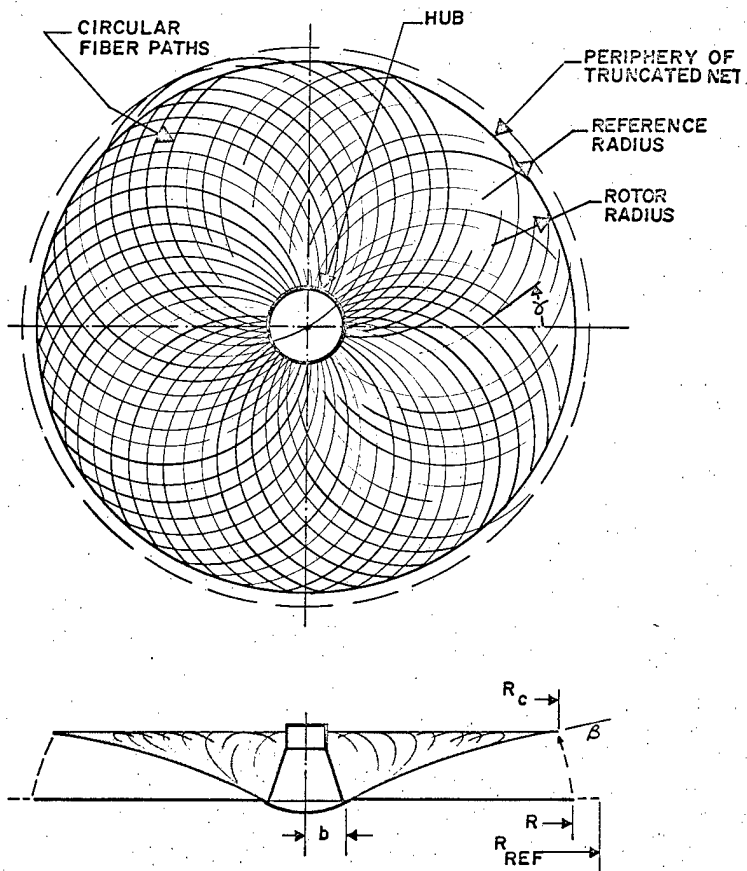


Figure 4. Adaptation of Isotensoid Disk to Rotonet

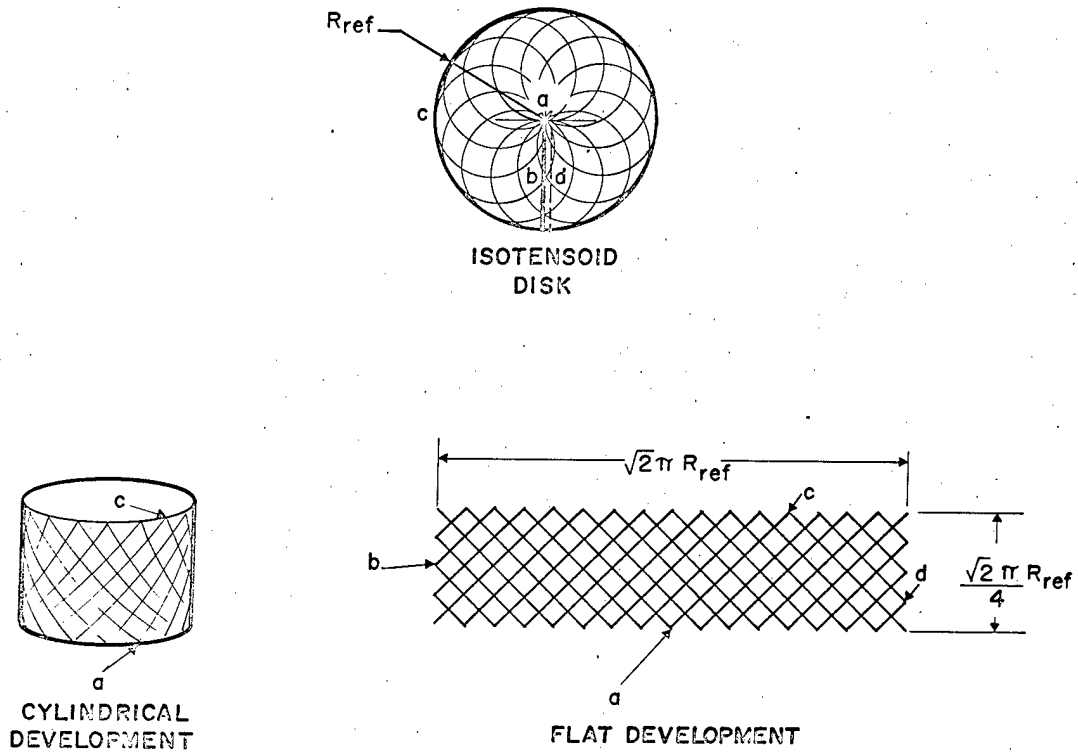


Figure 5. Geodesic Development of Isotensoid Disk

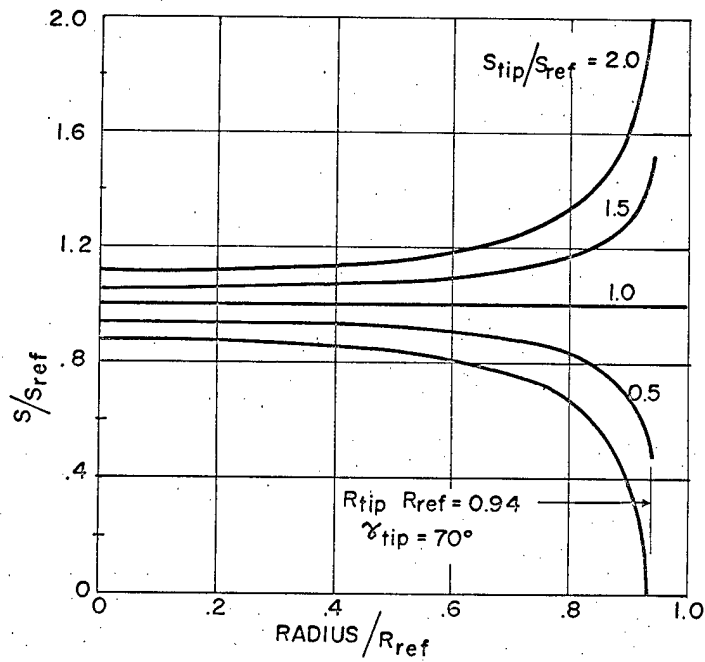


Figure 6. Stress Distribution in Truncated Disk With Various Sizes of Tip Weights

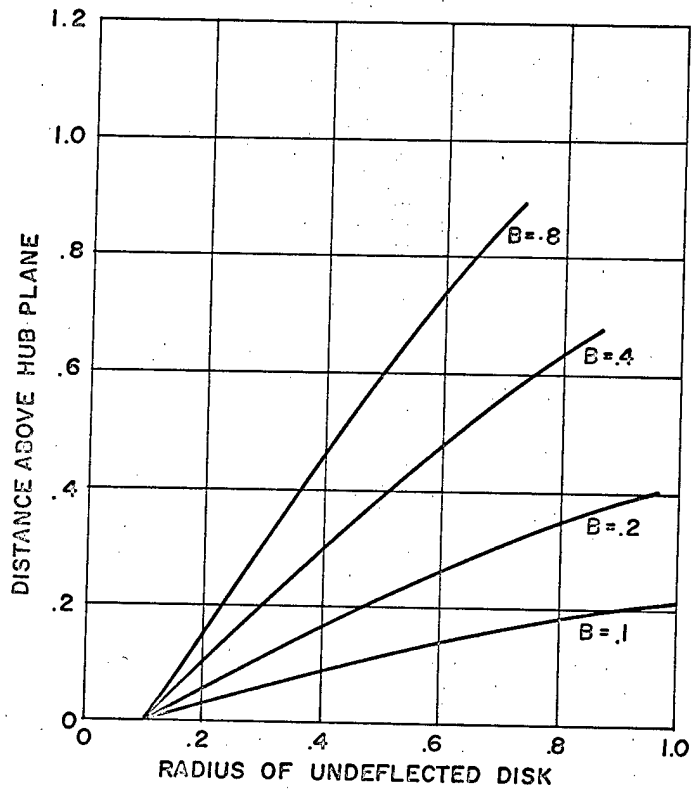


Figure 7. Meridional Curves for Coned-Up Rotornet

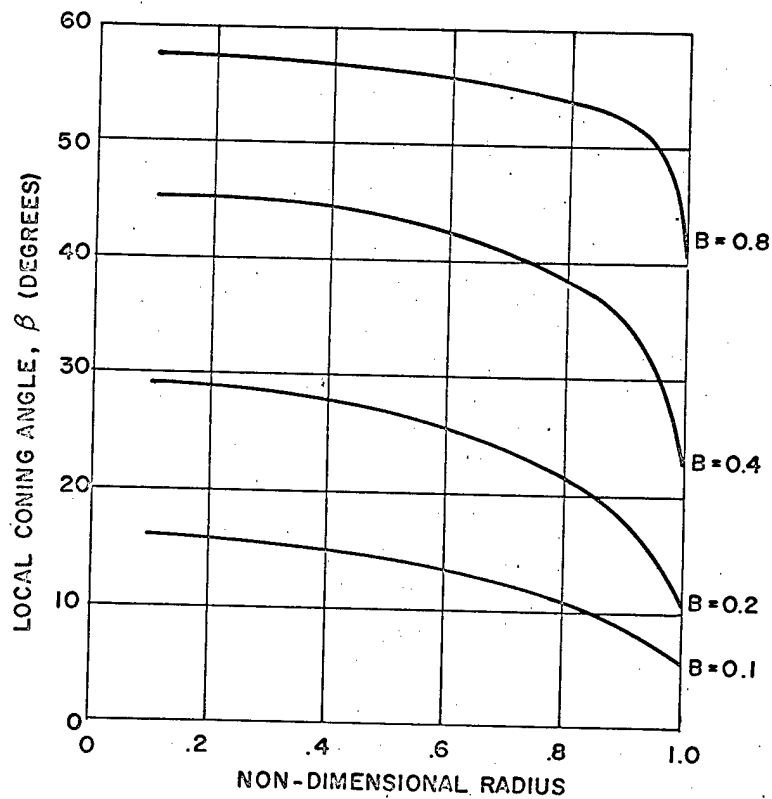


Figure 8. Coning Angle Distribution

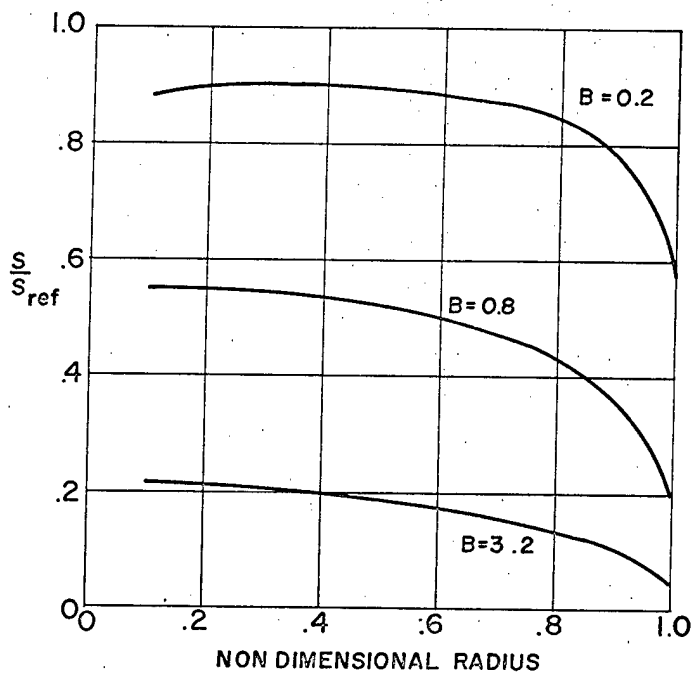


Figure 9. Tension Distribution

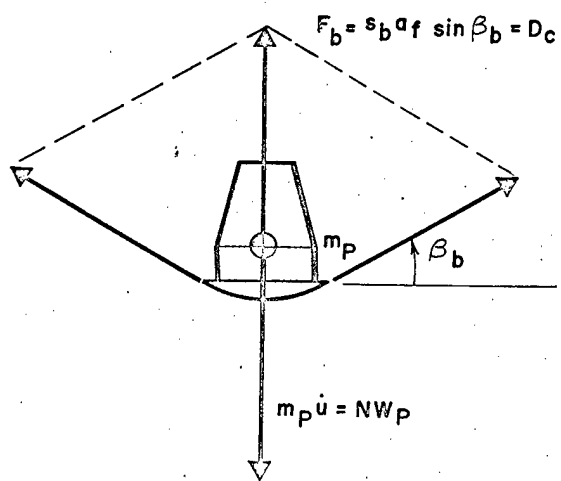


Figure 10. Axial Equilibrium at the Hub

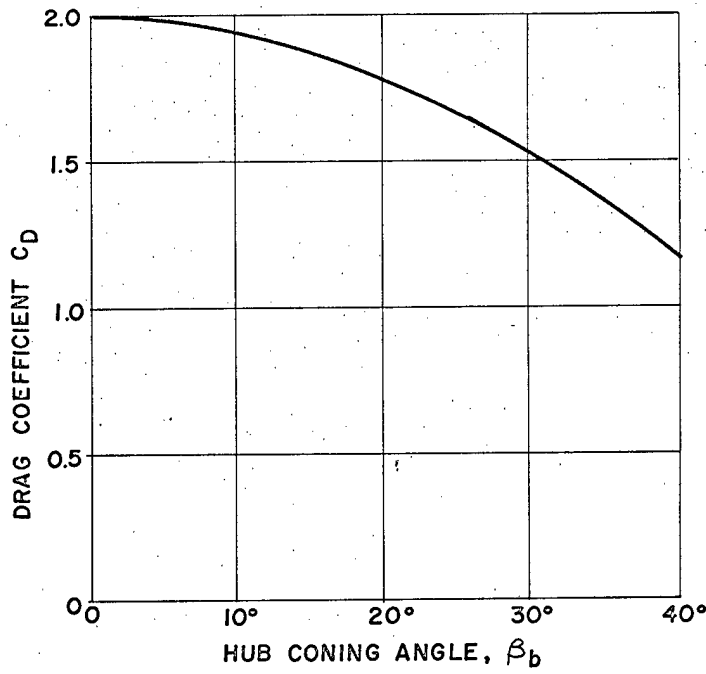


Figure 11. Drag Coefficient vs. Coning Angle
(Referred to area of flat disk)

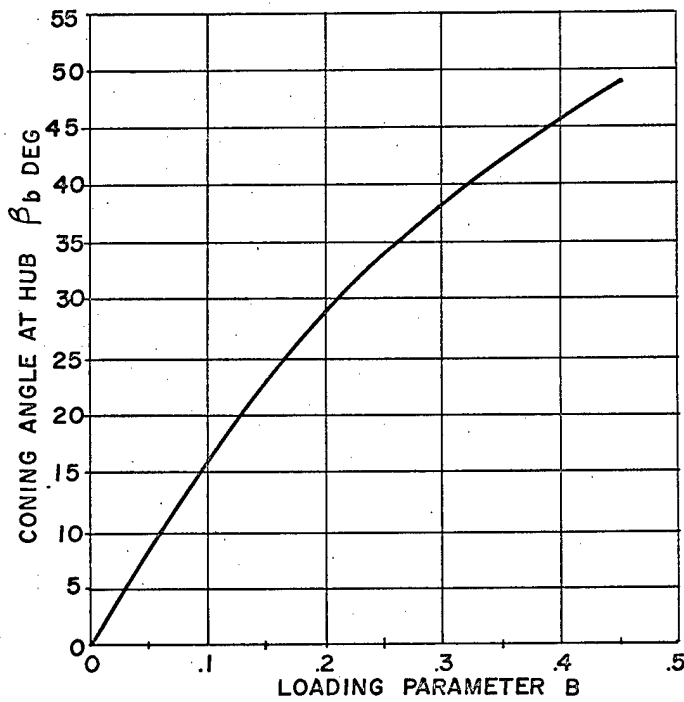


Figure 12. Coning Angle vs. Loading

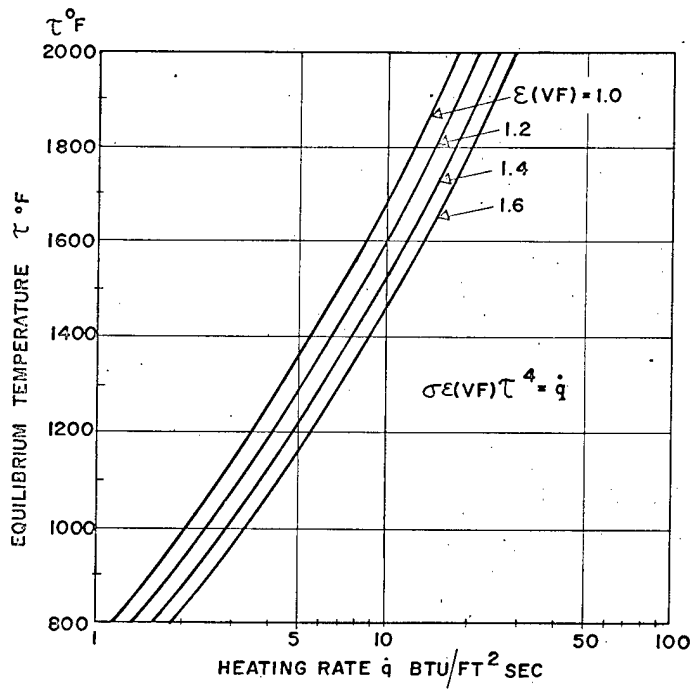


Figure 13. Equilibrium Temperature vs. Heating Rate

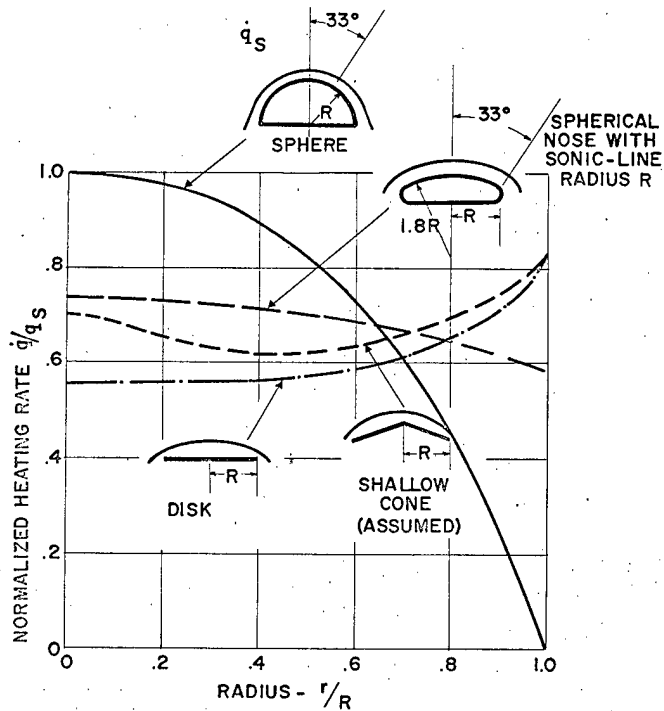


Figure 14. Heating Distributions for Blunt Shapes, Normalized to Stagnation-Point Heating on a Sphere

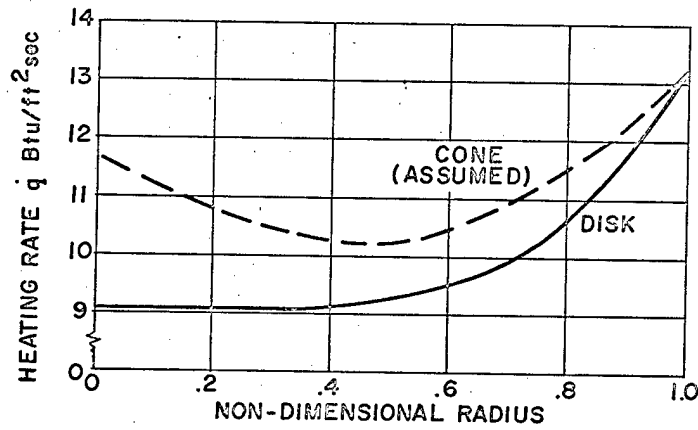
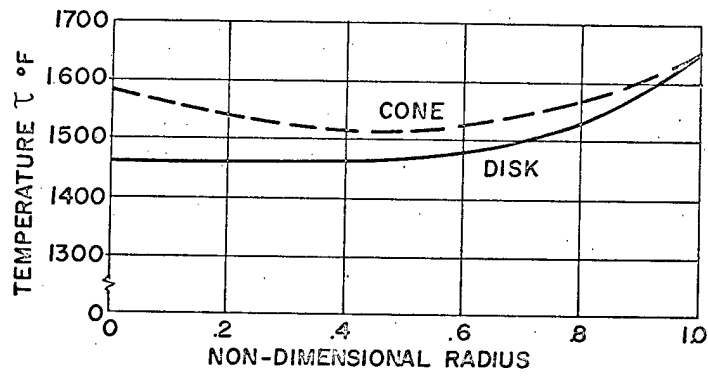


Figure 15. Heating Rate and Temperature Distributions on Disk and Shallow Cone

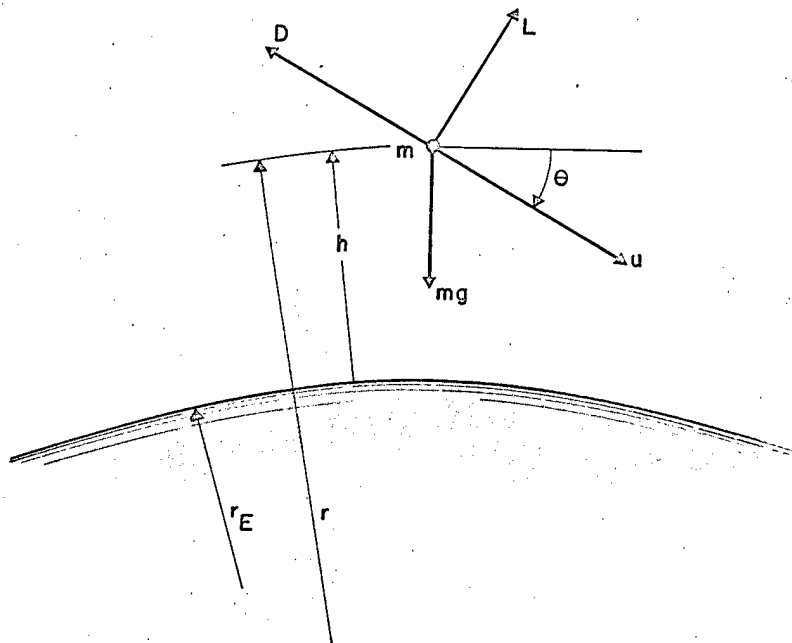
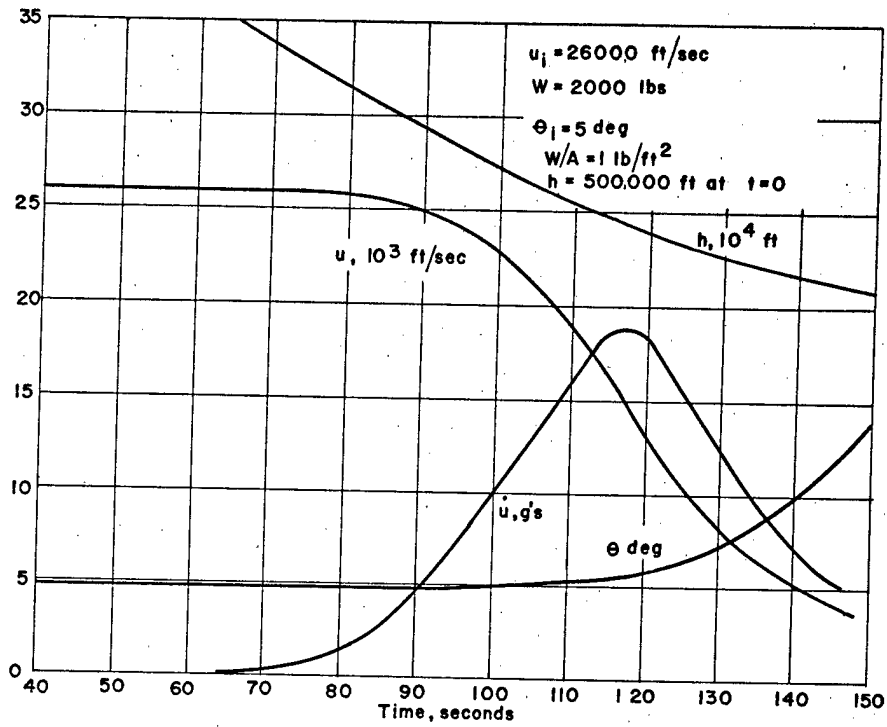
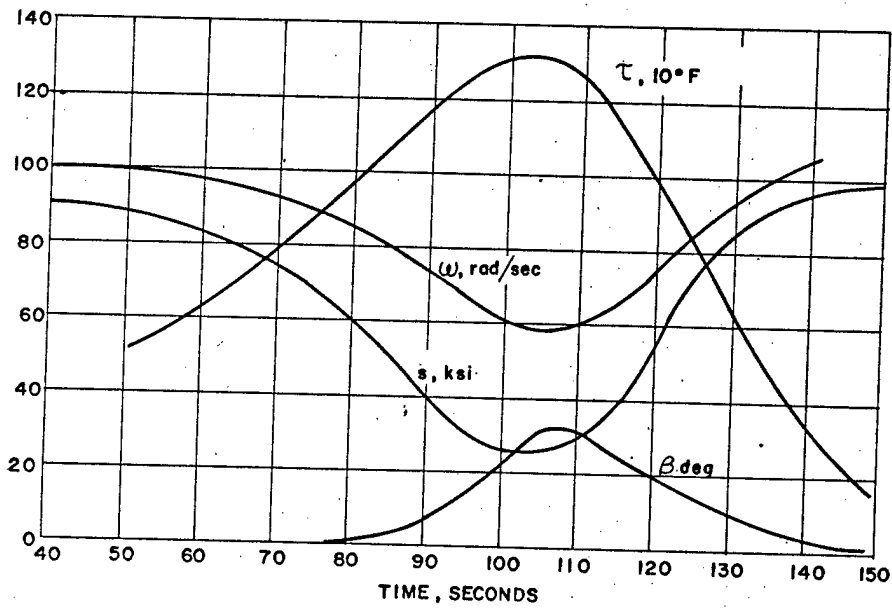


Figure 16. Coordinate System for Equations of Motion for Entry Vehicle



a. Vehicle Motion



b. Rotornet Response

Figure 17. Ballistic Trajectory for Earth Entry With Constant Margin of Safety

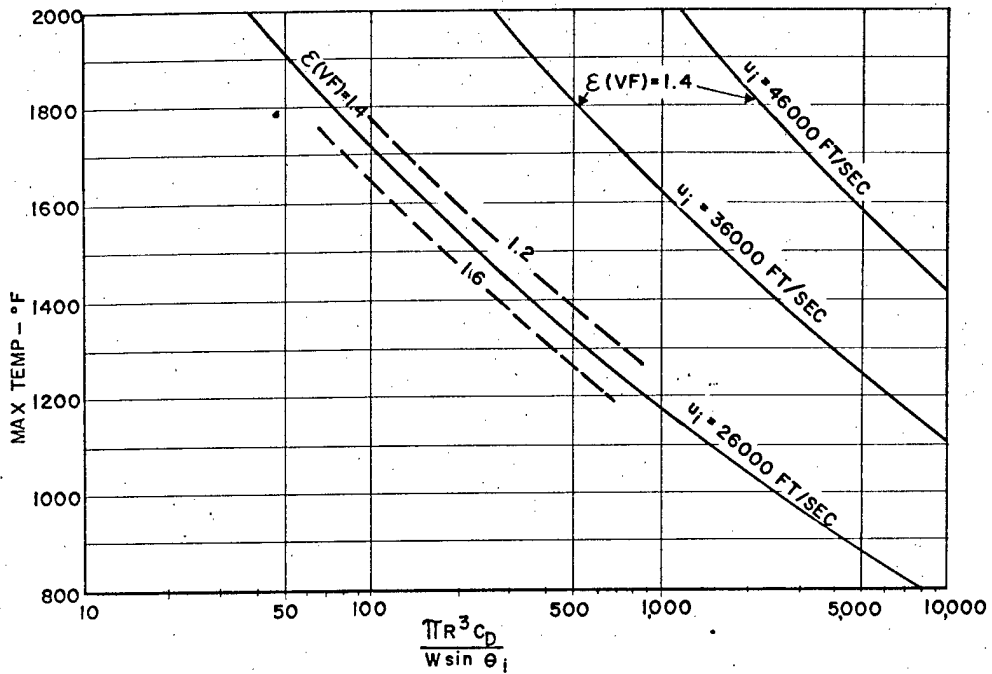


Figure 18. Maximum Temperature During Ballistic Entry vs. Heating Parameter.

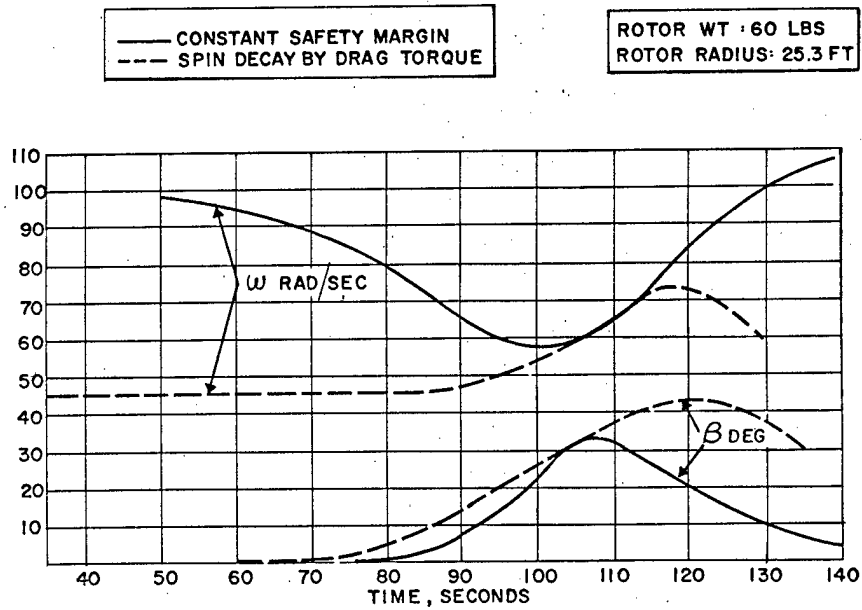


Figure 19. Spin Rate and Coning Angle for Spin Decay Operation Compared with Constant Margin Operation

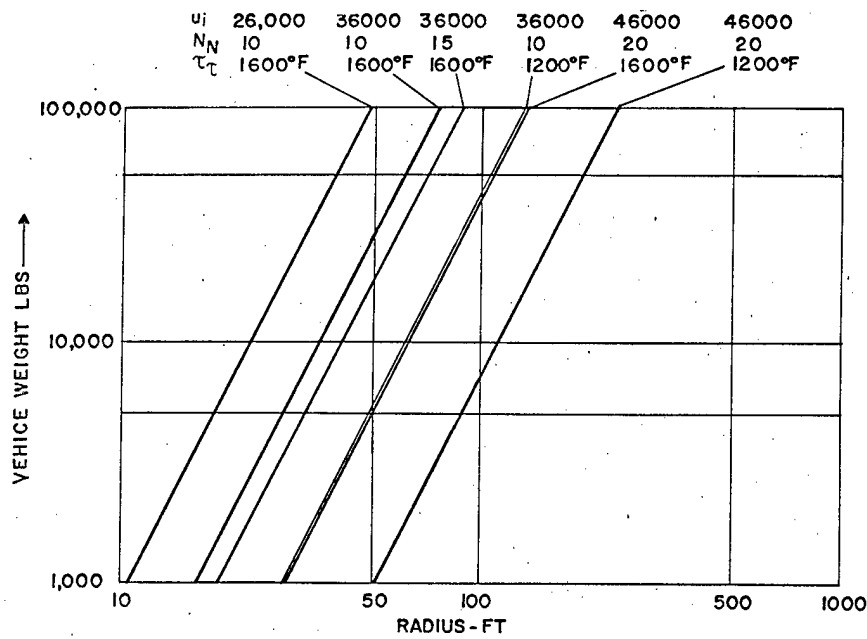


Figure 20. Rotonet Radius for Ballistic Entry

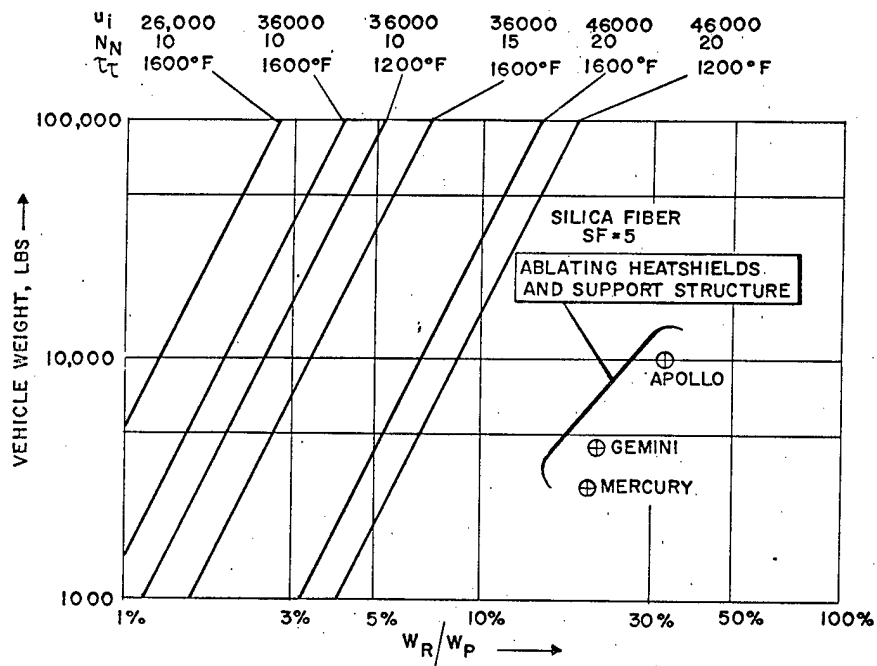


Figure 21. Rotonet Weight Fraction for Ballistic Entry
(Silica fiber with safety factor of 5)

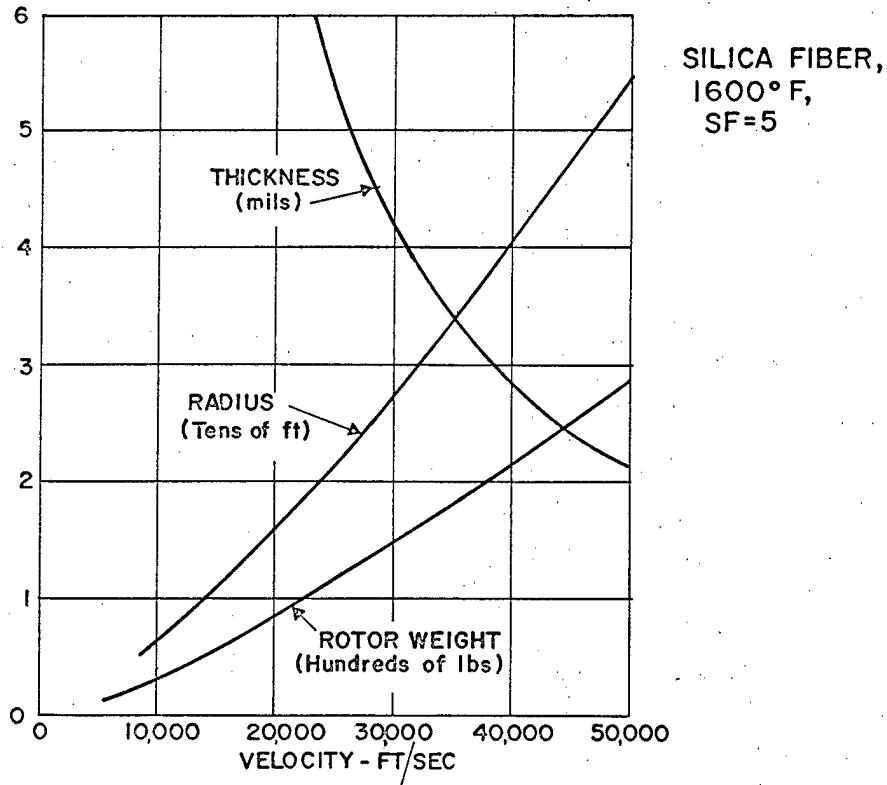


Figure 22. Rotor Size vs. Initial Velocity for 10,000 lb Vehicle (10 g's, 1600°F, Silica, SF=5)

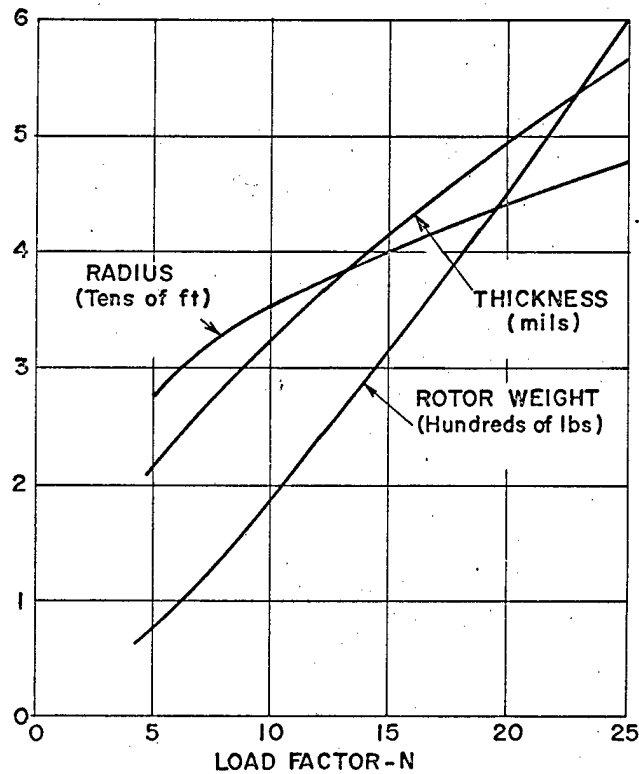


Figure 23. Rotor Size vs. Maximum Load Factor for 10,000 lb Vehicle (36,000 ft/sec, 1600°F, Silica, SF=5)

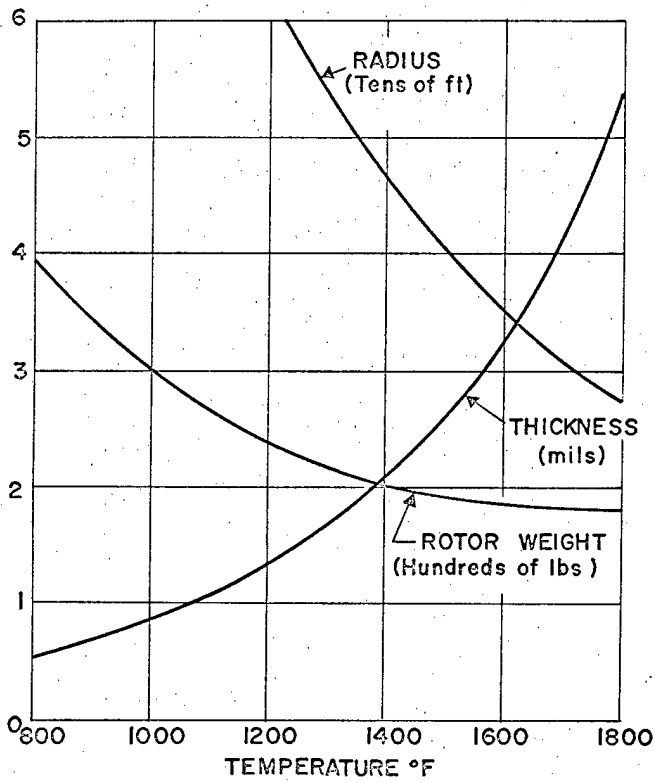


Figure 24. Rotornet Size vs. Maximum Temperature for 10,000 lb Vehicle (36,000 ft/sec, 10 g's, Silica, SF=5)

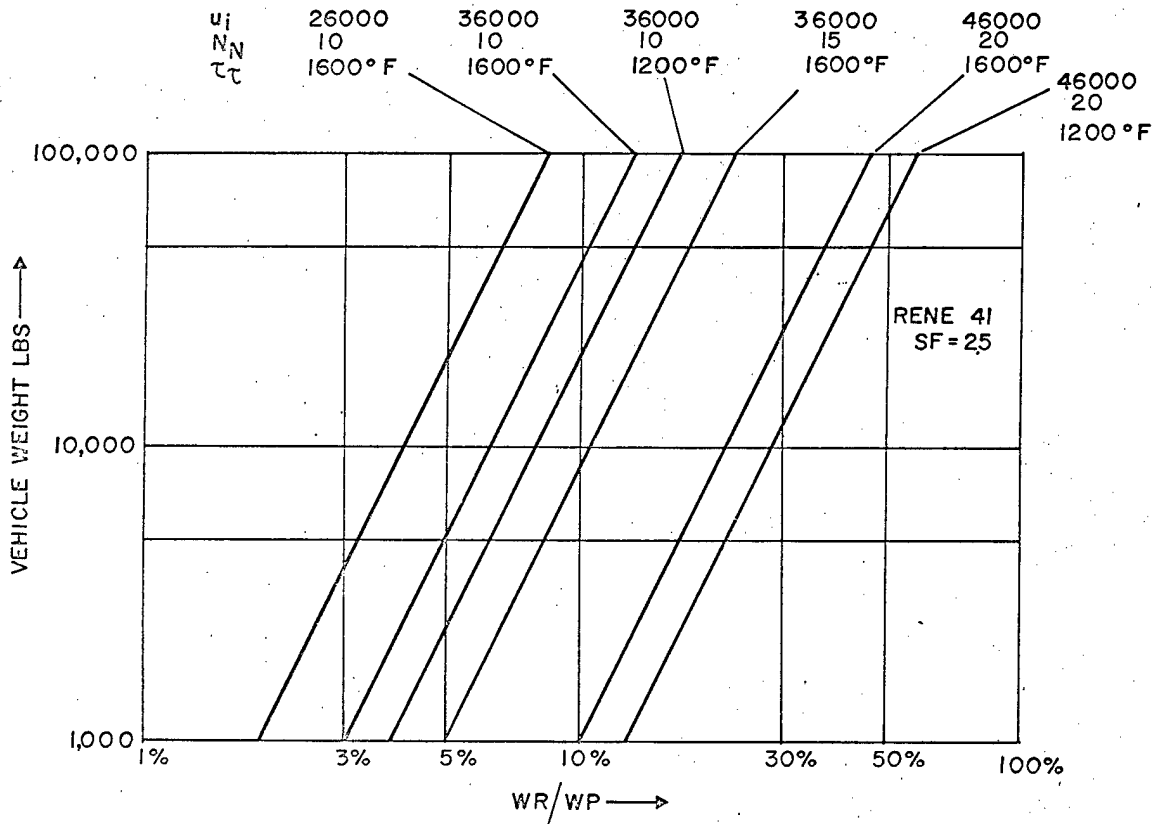


Figure 25. Rotornet Weight Fraction for Ballistic Entry (Rene' 41 with safety factor of 2.5)

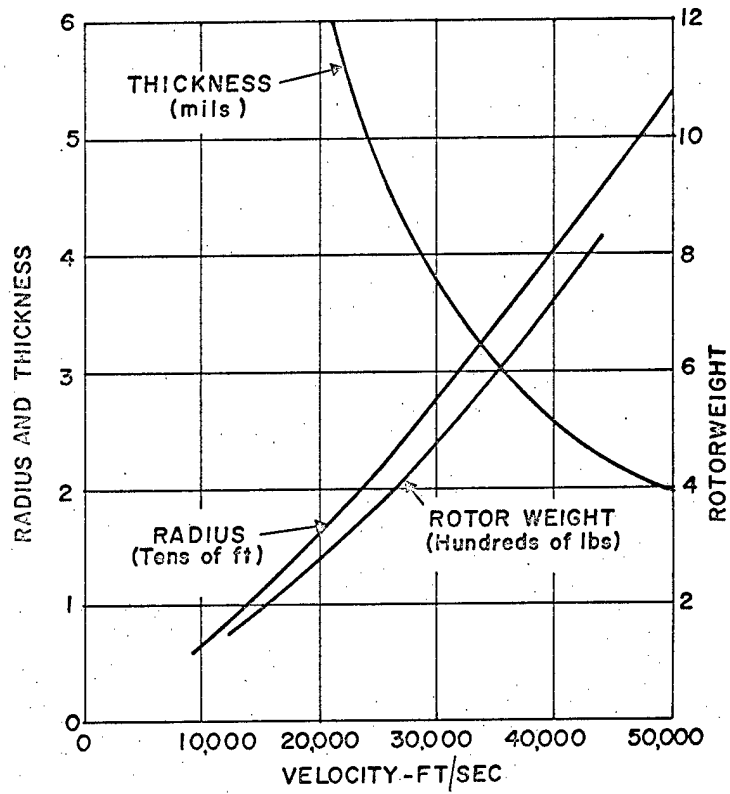


Figure 26. Rotor Size vs. Initial Velocity for 10,000 lb Vehicle (10 g's, 1600°F, Rene' 41, SF=2.5)

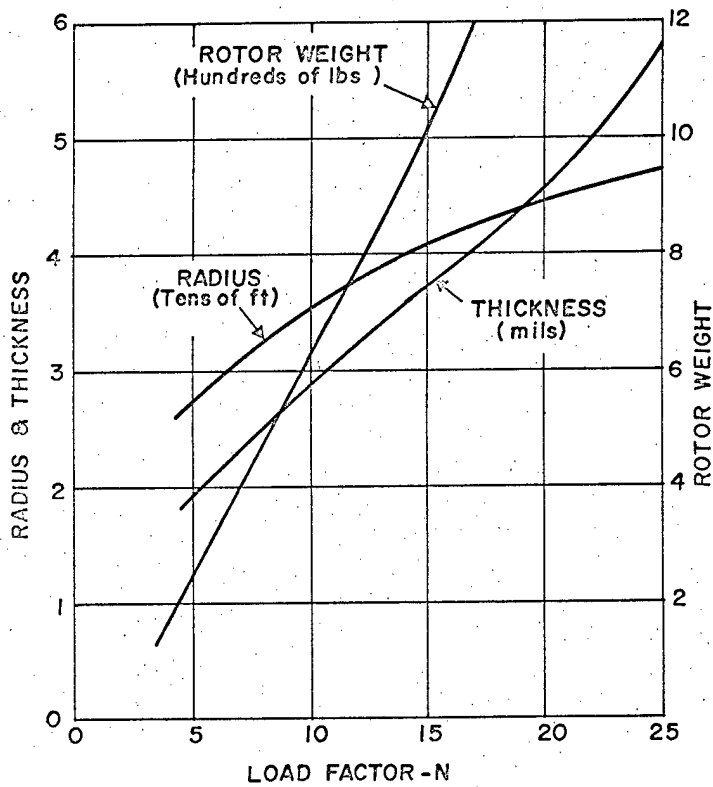


Figure 27. Rotor Size vs. Maximum Load Factor for 10,000 lb Vehicle (36,000 ft/sec, 1600°F, Rene' 41, SF=2.5)

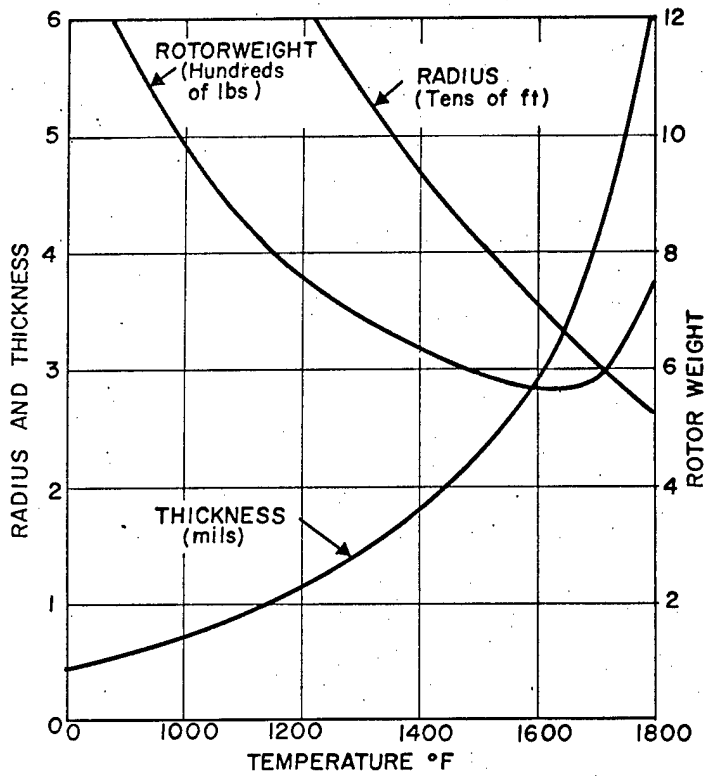


Figure 28. Rotornet Size vs. Maximum Temperature for 10,000 lb Vehicle (36,000 ft/sec, 10 g's, Rene' 41, SF=2.5)

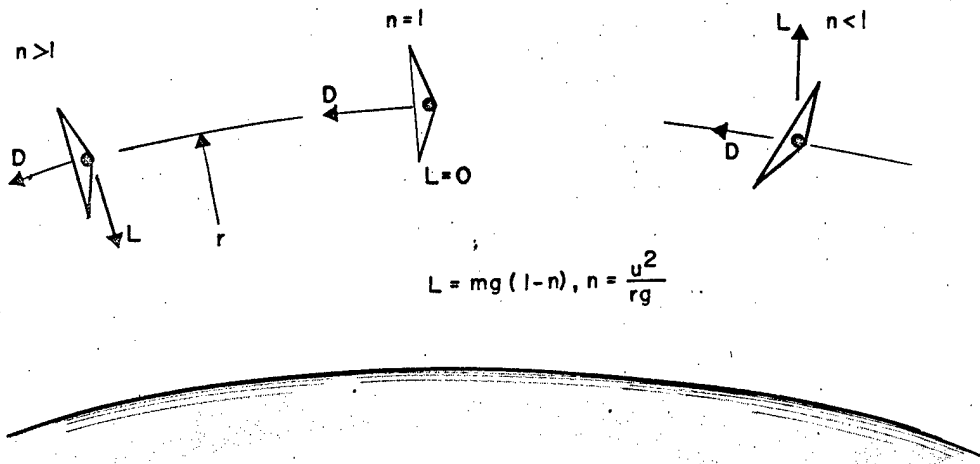


Figure 29. Conditions for Equilibrium Glide

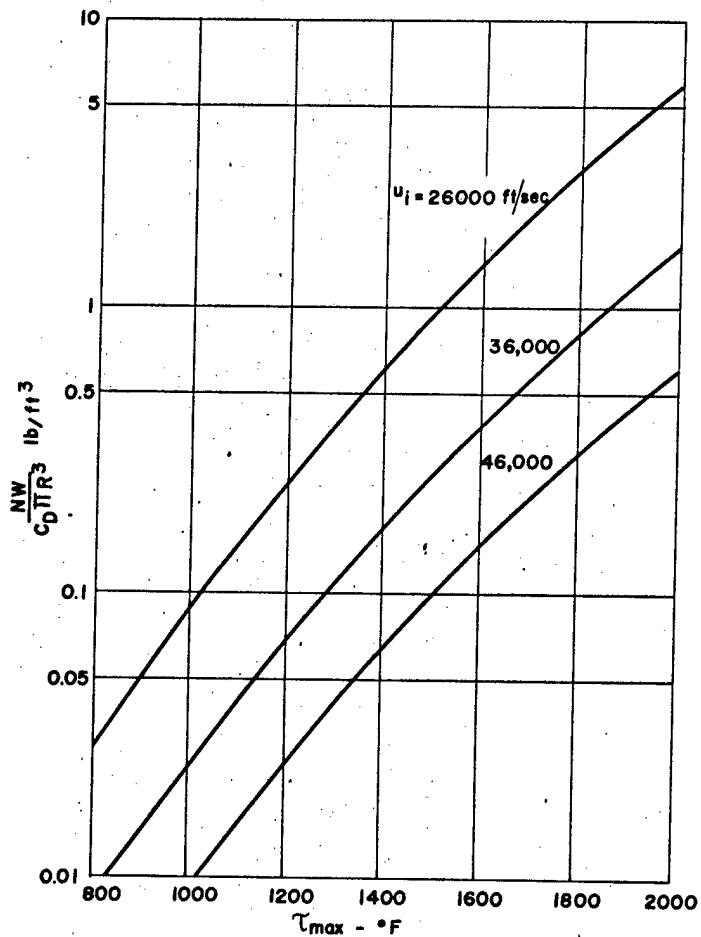


Figure 30. Maximum Temperature vs. Load Density

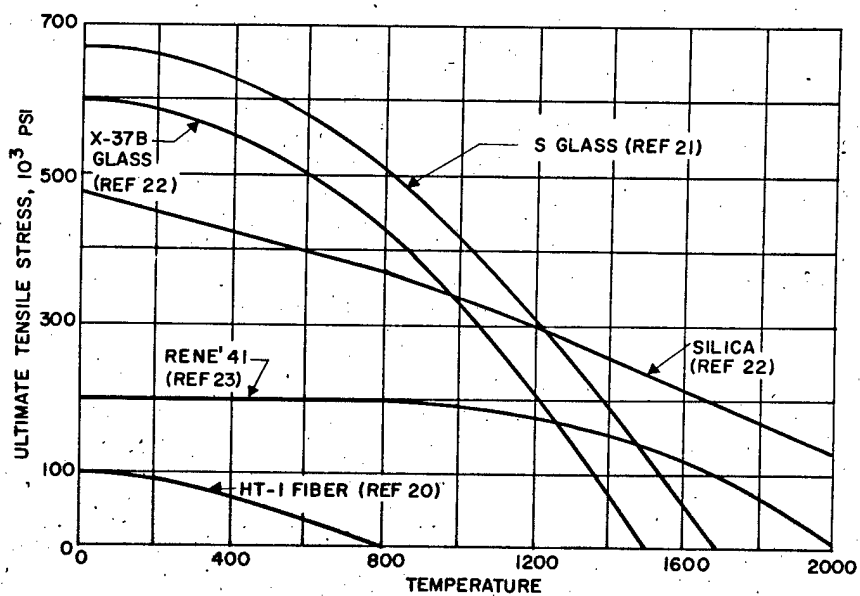


Figure 31. Strength vs. Temperature for Structural Fibers

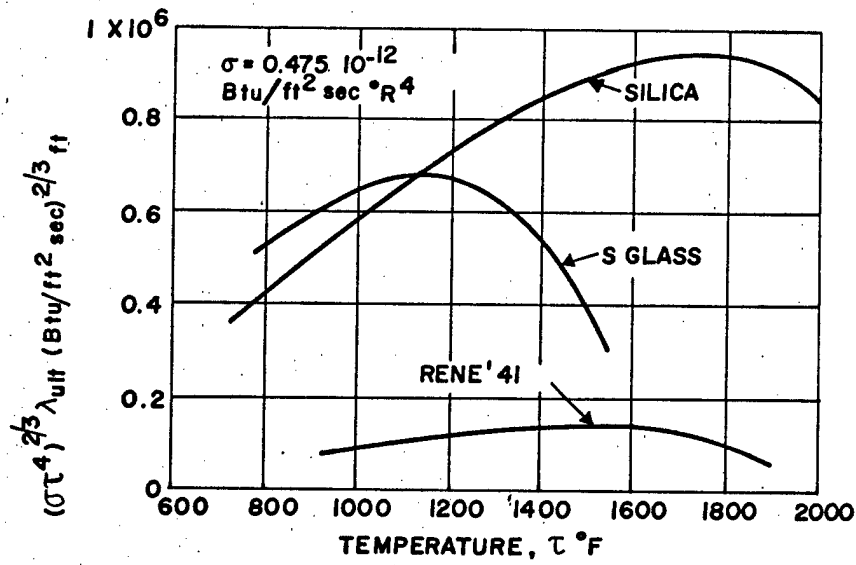


Figure 32. Temperature-Weight Performance Parameter $(\sigma\tau)^{4/3} \lambda_{ult}$ vs. Temperature

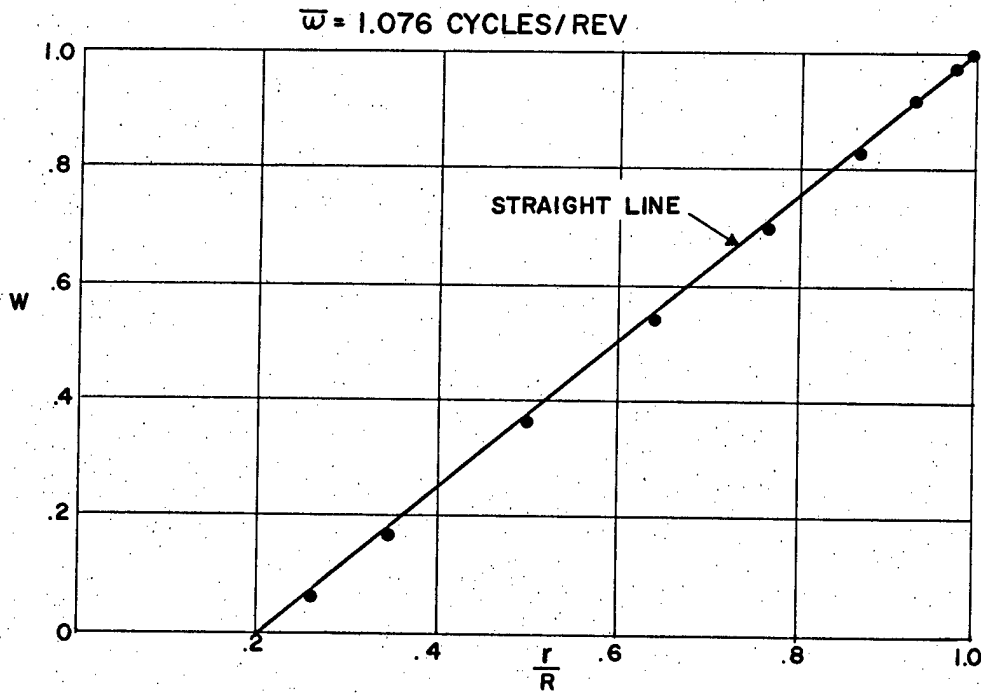


Figure 33. Out-of-Plane Vibration of a Flat Isotensoid Disk: Mode Shape for First Mode

$\bar{\omega} = 1.26$ CYCLES/REV.

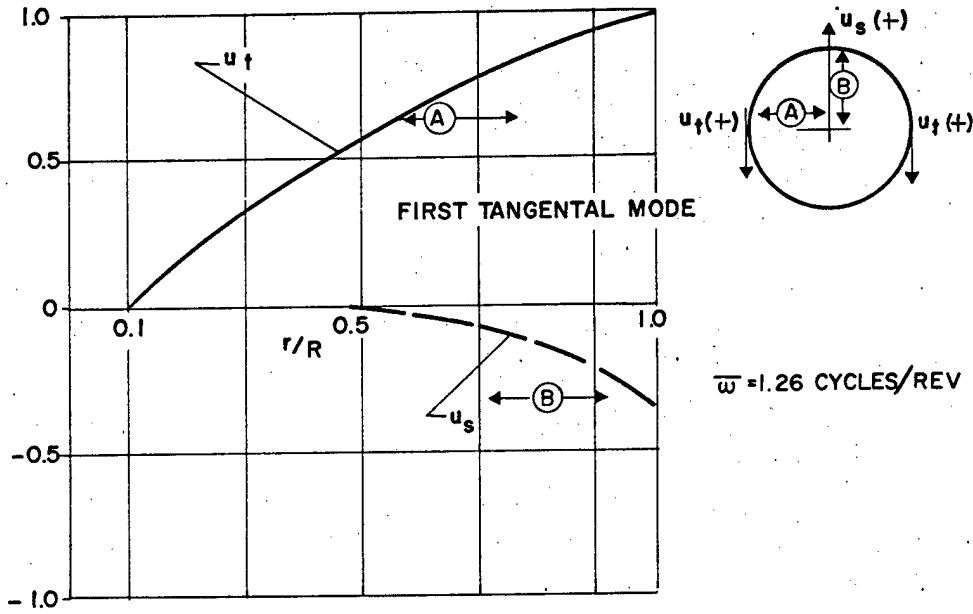


Figure 34. In-Plane (tangential) Vibration of a Flat Isotensoid Disk: Mode Shape for First Mode

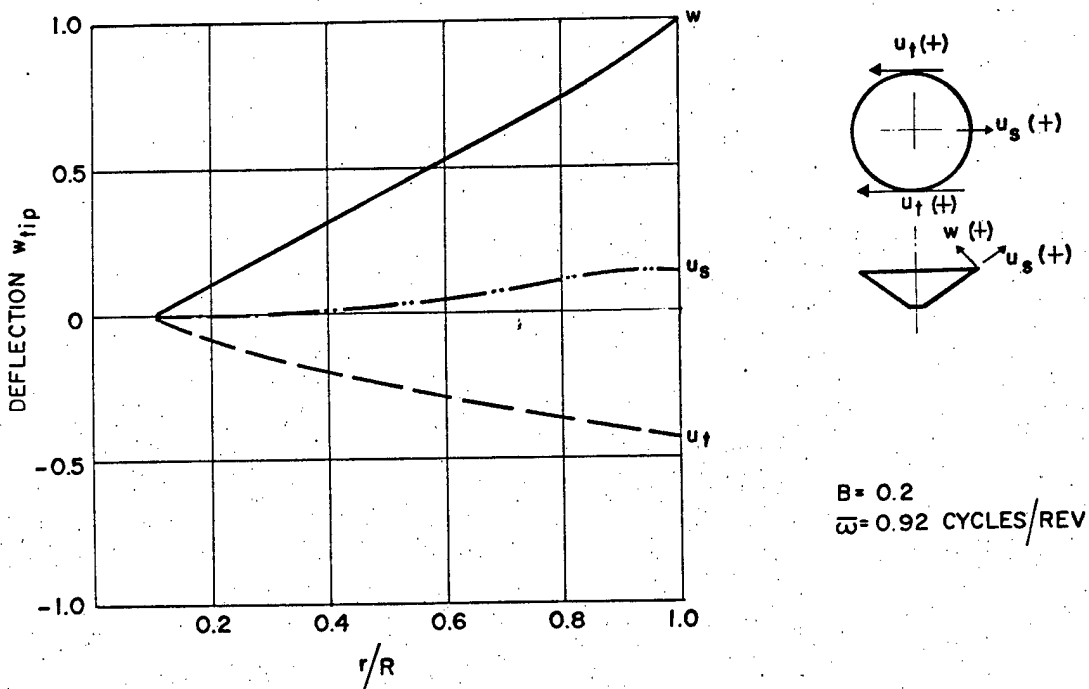


Figure 35. Vibration of a Coned-Up Rotornet: Mode Shape for First Flapping Mode

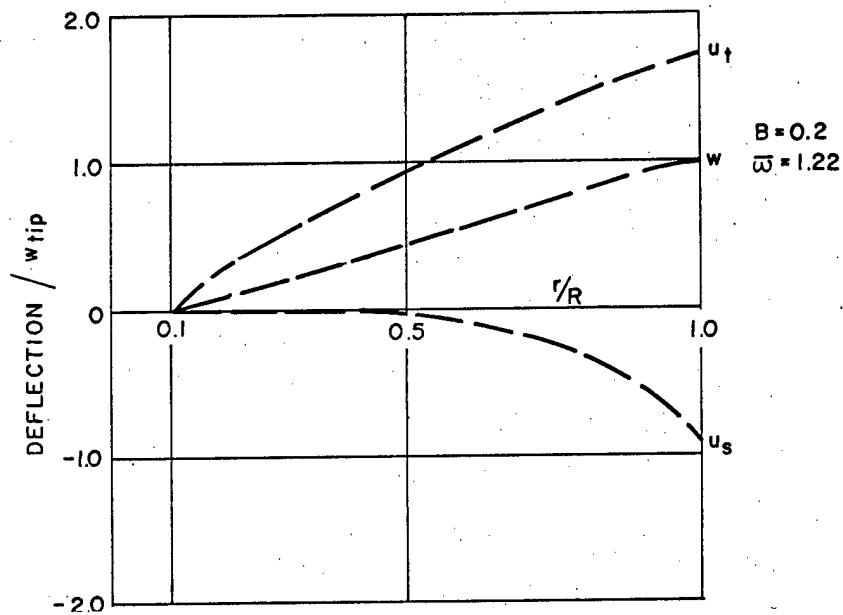


Figure 36. Vibration of a Coned-Up Rotornet: Mode Shape for First Tangential Mode

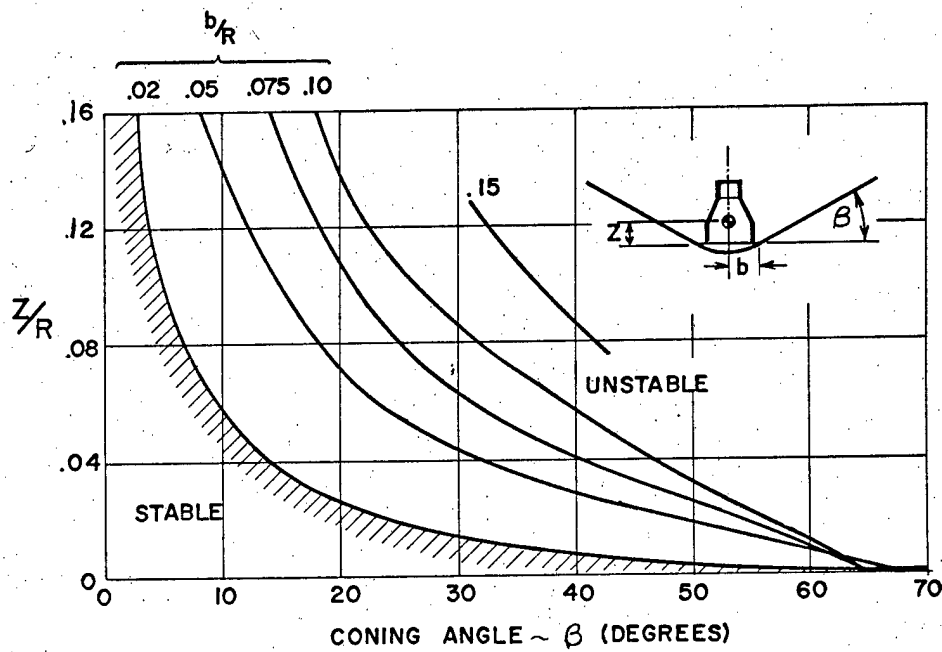


Figure 37. Boundary for Catastrophic Flutter

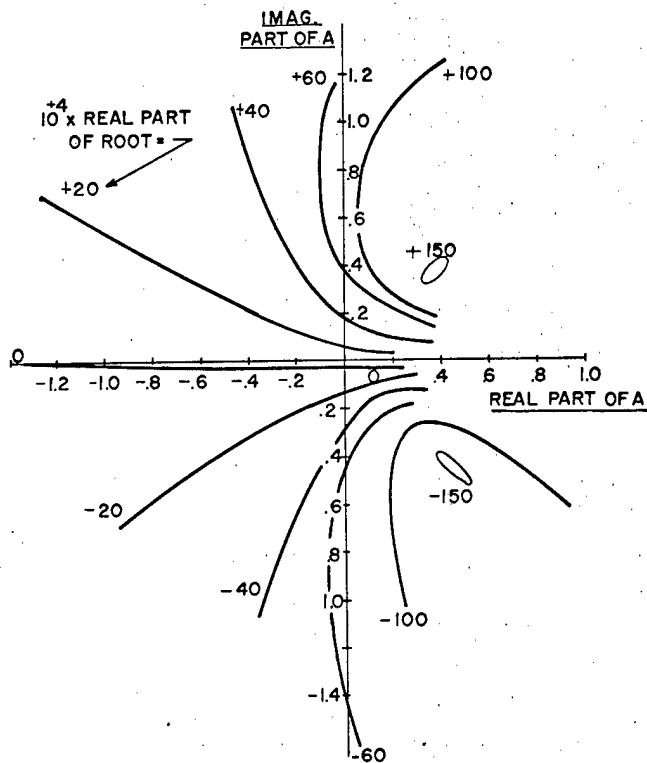


Figure 38. Effect of Actuator Gain on Stability of Spiral Mode

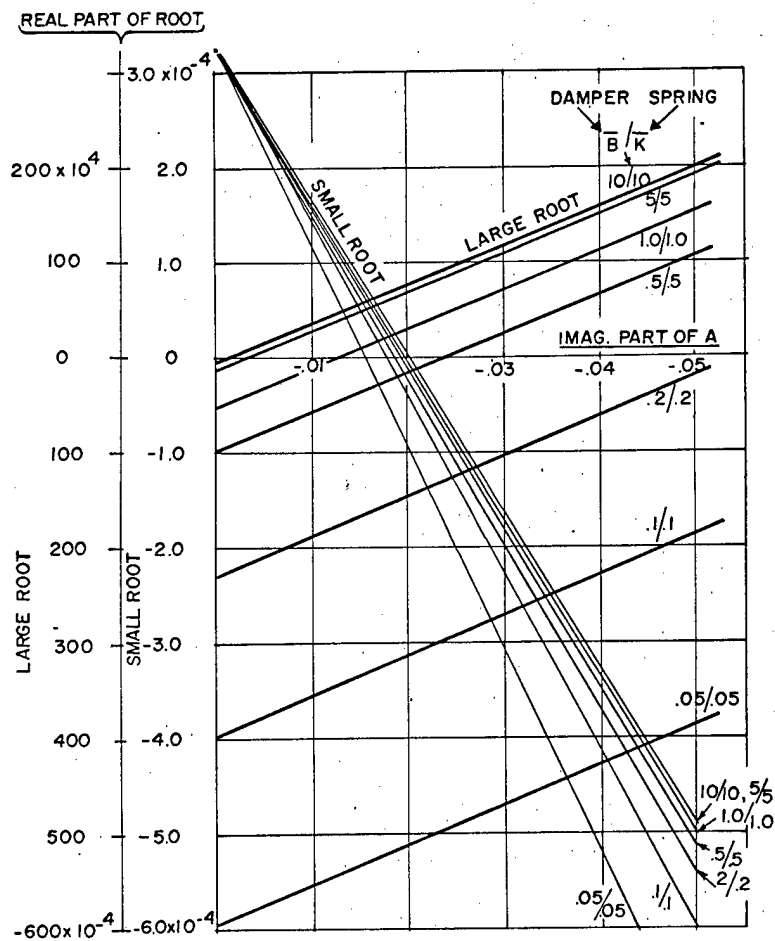


Figure 39. Effect of Stability Augmentation Parameters

NET CONSTRUCTION DETAIL

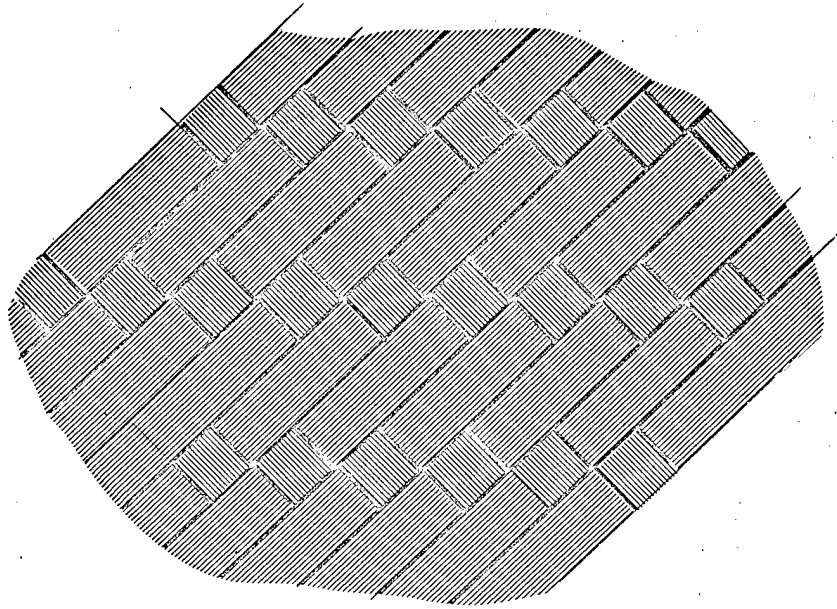


Figure 40. Typical Basket-Weave Construction with Parallel Fiber Tapes

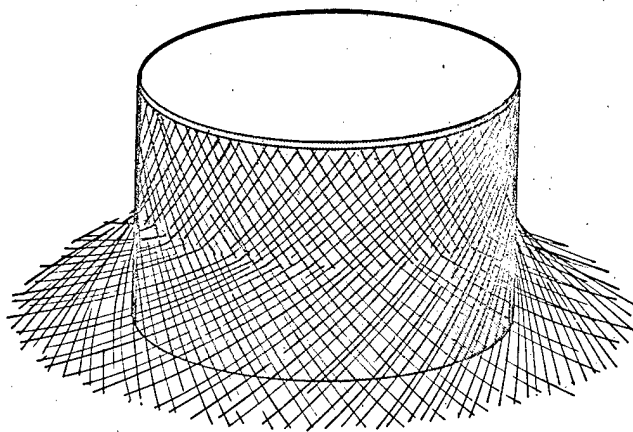


Figure 41. Fabrication of Rotinet by Basket-Weaving Tapes on a Cylinder Form.

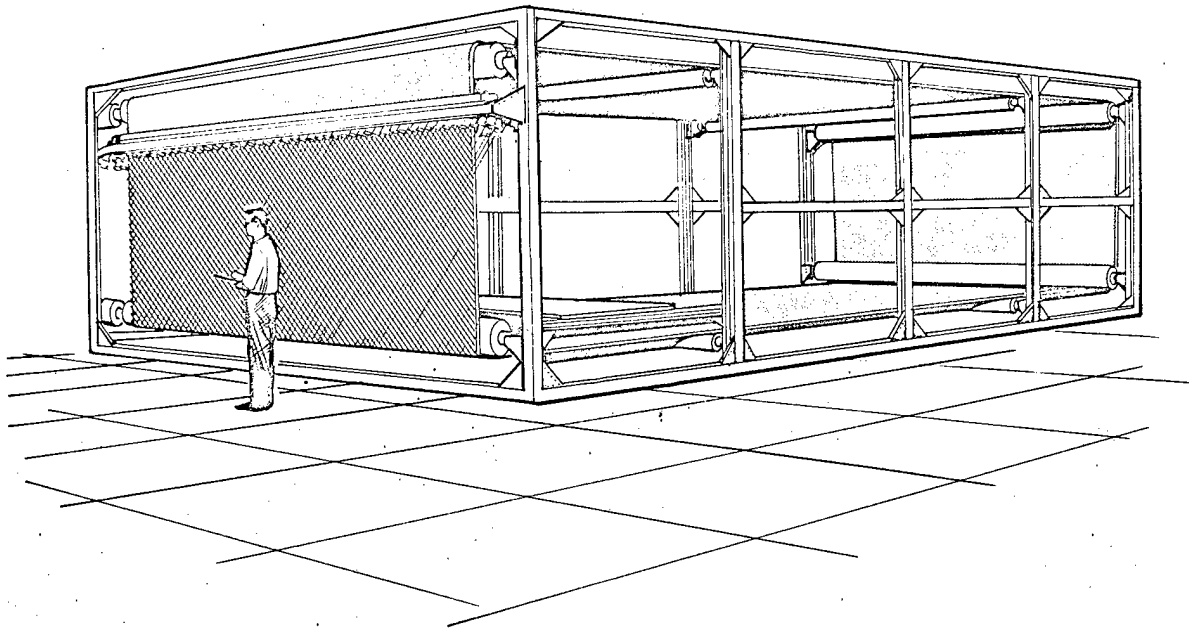


Figure 42. Fabrication of Rotornet by Braiding Tapes on a Continuous Belt

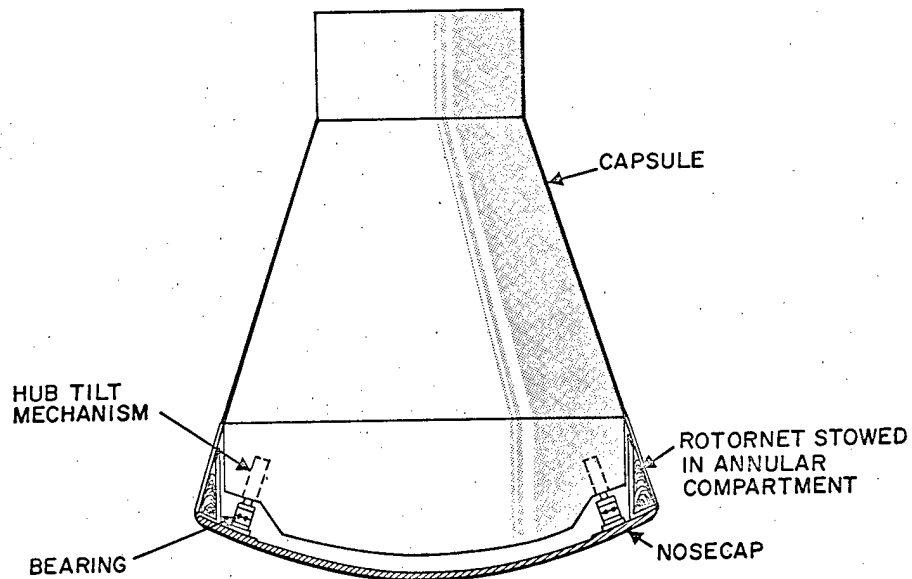


Figure 43. Rotating Hub Structure

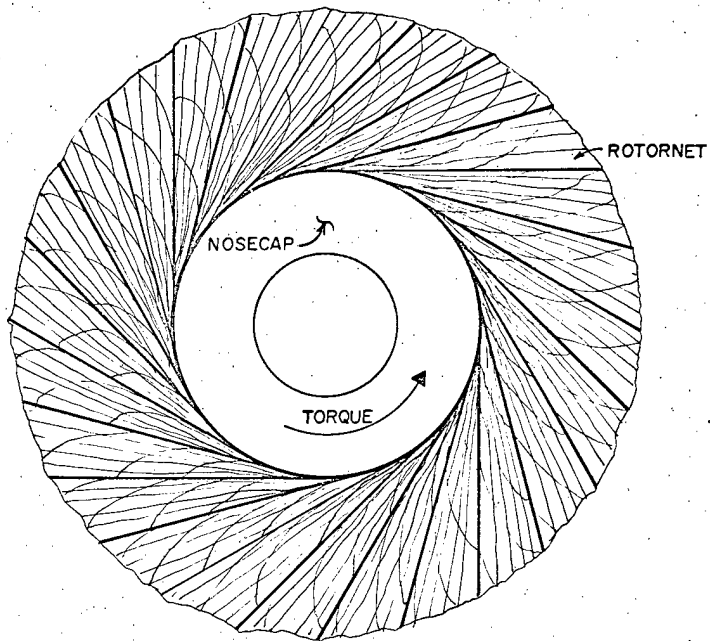


Figure 44. Deployment of Rotornet

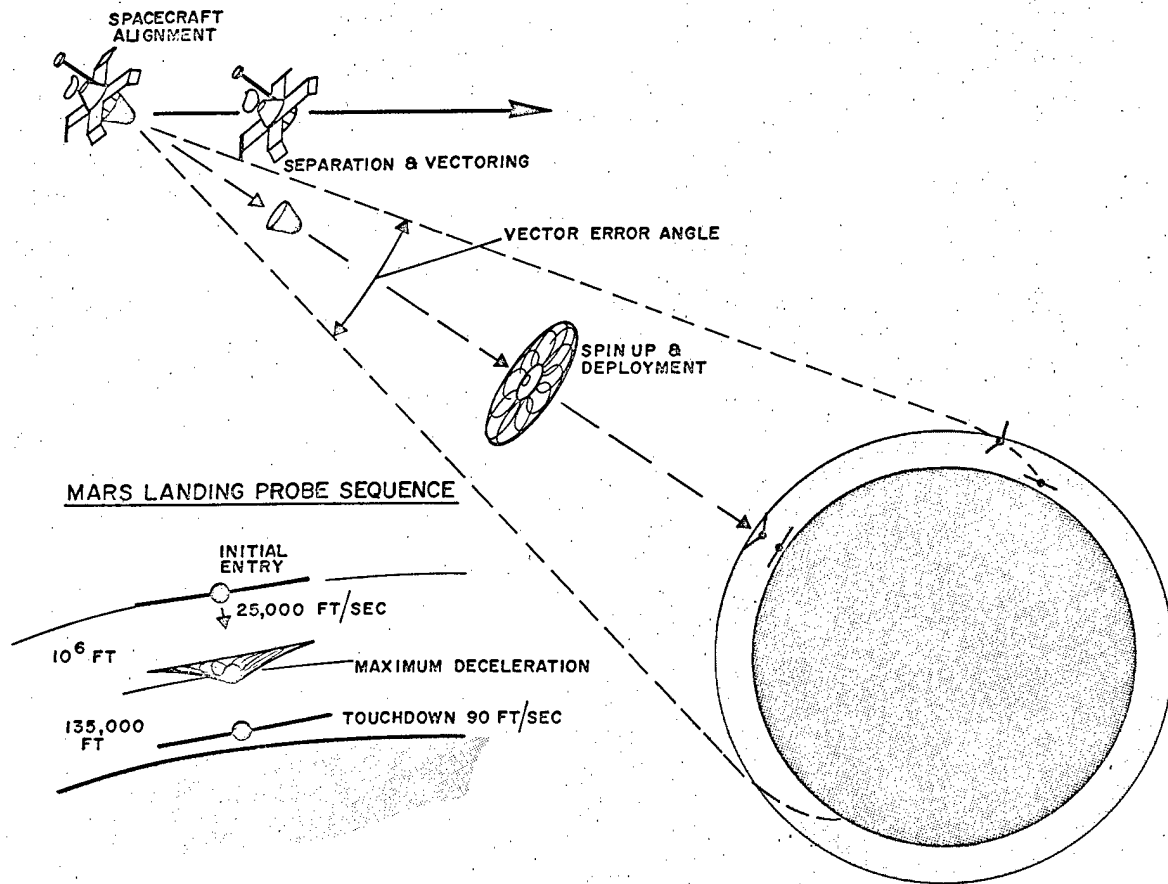


Figure 45. Mars Landing Probe Mission

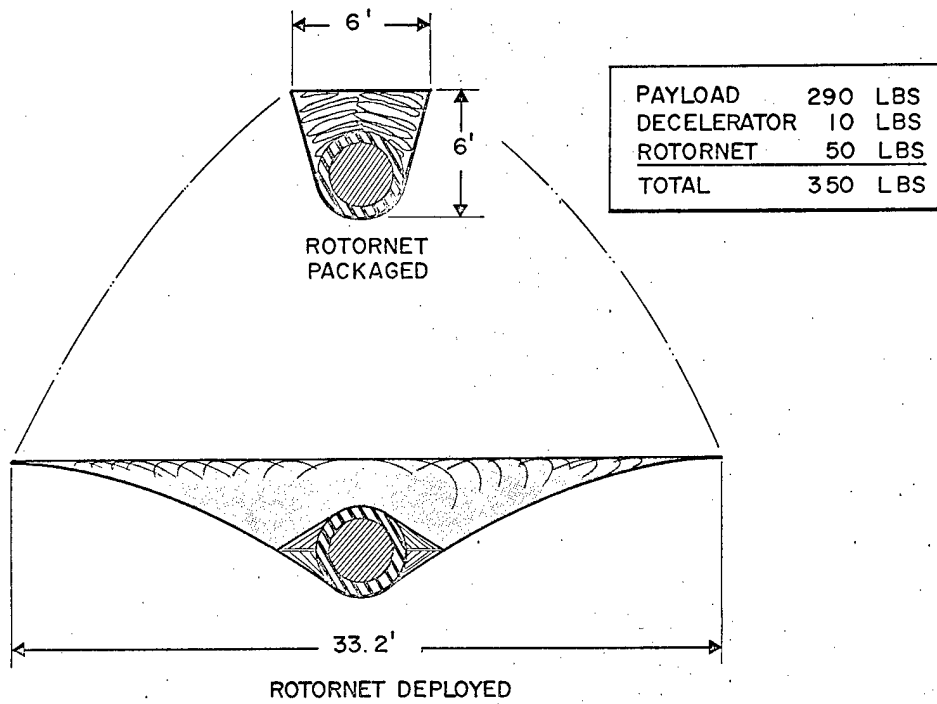


Figure 46. Rotornet Design for Entry on Mars at 90° and 25,000 ft/sec.

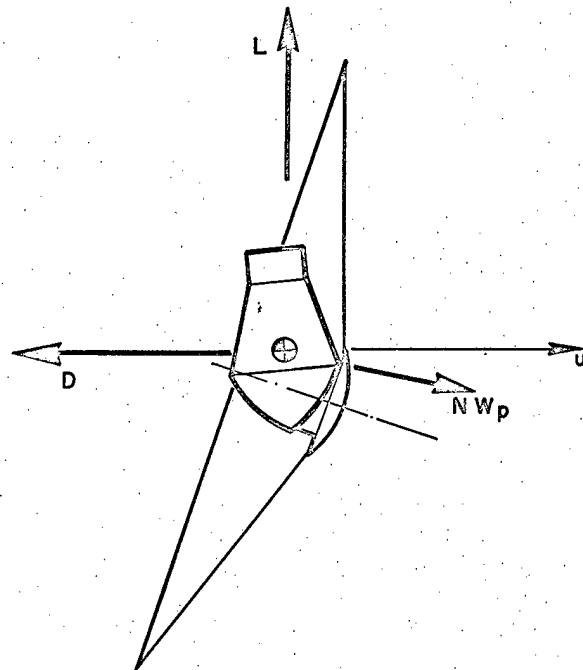


Figure 47. Fixed-Offset Glide Vehicle